J. Fluid Mech. (2019), *vol.* 862, *pp.* 34–74. © Cambridge University Press 2019
doi:10.1017/jfm.2018.911

Hydrodynamics of periodic wave energy converter arrays

Grgur Tokić[1] **and Dick K. P. Yue**[1,†]

[1]Department of Mechanical Engineering, Massachusetts Institute of Technology, Cambridge, MA 02139, USA

(Received 29 June 2018; revised 25 October 2018; accepted 6 November 2018; first published online 4 January 2019)

We consider the hydrodynamics of wave energy converter (WEC) arrays consisting of periodically repeated single bodies or sub-arrays. Of special interest is the array gain due to wave interactions as a function of the spatial configuration of the array. For simplicity, we assume identical WECs oscillating in heave only, although the results should extend to general motions. We find that array gains can be as high as $O(10)$ compared to the same WECs operating in isolation. We show that prominent decreases in array gain are associated with Laue resonances, involving the incident and scattered wave modes, for which we obtain an explicit condition. We also show theoretically that Bragg resonances can result in large decreases in gain with as few as two rows of strong absorbers. For general WEC geometries, we develop a multiple-scattering method of wave–body interactions applicable to generally spaced periodic arrays. For arrays of truncated vertical cylinders, we perform numerical investigations confirming our theoretical predictions for Laue and Bragg resonances. For a special class of multiple-row rectangular WEC arrays, our numerical results show that motion-trapped Rayleigh–Bloch waves can exist and be excited by an incident wave, resulting in sharp, narrow-banded spikes in the array gain.

Key words: surface gravity waves, wave scattering, wave–structure interactions

1. Introduction

Among the myriad of currently available concepts for ocean wave energy extraction (Drew, Plummer & Sahinkaya 2009; Babarit 2015), there is still no consensus as to which one offers the greatest potential for practical implementation. We focus here on energy extraction by oscillating buoys placed in close proximity to each other to form wave energy converter (WEC) arrays; this concept offers a realistic and practical approach for achieving industrial-level wave energy harvesting. A particularly attractive aspect of this system is that carefully designed WEC arrays could offer a possibility of significantly improving the energy extraction performance over the same number of isolated extractors.

Most of the proposed or existing WEC arrays have converters placed in a lattice-like arrangement, usually forming a (finite-size) square or a rectangular lattice (e.g. Weller, Stallard & Stansby 2010; Stratigaki *et al.* 2014). This spatial arrangement makes it

† Email address for correspondence: yue@mit.edu

https://doi.org/10.1017/jfm.2018.911 Published online by Cambridge University Press

particularly suitable to model these as periodic arrays, especially as the number of bodies grows along one direction. However, our understanding of the performance of periodic WEC arrays and the physics that describes it is lacking when compared to that of other periodic systems immersed in a wave-supporting medium (e.g. photonic crystals in optics (Joannopoulos *et al.* 2008), phononic crystals in acoustics (Craster & Guenneau 2013)).

Theoretical analysis of WEC array performance was first conducted for point absorbers (Evans 1980; Falnes 1980) – idealized energy extractors that do not scatter waves, but respond to the resultant wave field created by the incident wave and radiated waves from each of the extractors. An appealing feature of the point-absorber approach is that it obtains the optimal array gain solely based on the spatial configuration of the bodies, without requiring specification of body properties. Srokosz (1980) was the first to apply the point-absorber approximation to calculate the performance of a periodic WEC array, deriving the maximum gain of an infinite row of point absorbers for normal incidence. Falnes & Budal (1982) and Falnes (1984) generalized the result by Srokosz for rectangular periodic arrays and arbitrary incidence angles. They showed that abrupt changes in array gain occur at wavelengths where new scattering modes emerge from the array. While relevant for optimal (usually large amplitude) motion, for non-optimal motion (or strongly scattering devices) the point-absorber approximation leads to large errors due to the neglected scattered waves (McIver 1994). These shortcomings were somewhat rectified in the multiple-scattering approach based on the plane-wave approximation (Simon 1982), which includes the finite-size body effects and non-optimal motion, but relies on the far-spacing assumption and is formulated only for finite-sized arrays of axisymmetric heaving bodies.

Garnaud & Mei (2009, 2010) included the body effects by using multiple-scale analysis and homogenization theory to study the energy extraction by a large number of rows of small, weakly absorbing bodies (small relative to the wavelength). The spacing between the rows is uniform, and both the spacing and the periodicity are assumed to be large and of the same order of magnitude as the wavelength. They found that there is a substantial decrease in energy extraction in the vicinity of Bragg resonances. However, weakly absorbing buoys are economically ineffective, and the required assumptions on spacings and the number of rows limit the applicability of the theory to more general problems of practical interest.

An approach that in principle does not involve any approximations of the wave scattering and interaction problem is based on multiple-scattering theory (Kagemoto & Yue 1986). It is regularly used to calculate the performance of finite-size WEC arrays (e.g. Child & Venugopal 2010), but a formulation for periodic WEC arrays is currently missing. For non-WEC arrays, Peter, Meylan & Linton (2006) expanded the multiple-scattering framework to calculate the performance of a single periodic row of fixed or floating objects. Peter & Meylan (2009) later extended the theory using reflection and transmission matrices of a row as a whole to study the energy transfer across multiple periodic rows of bodies spaced far apart. Bennetts & Squire (2009) used a similar transfer-matrix approach for multiple periodic rows of floating bodies, but they were able to account for closely spaced rows and include both propagating and evanescent modes. However, the transfer-matrix approach is not well suited for analysis of WEC arrays because it lacks the ability to calculate the performance of particular bodies in the array (e.g. body motions, forces), which is of interest to actual design.

Our current understanding of periodic WEC array performance is thus largely limited to the effects of scattering mode creation and Bragg resonances on energy

https://doi.org/10.1017/jfm.2018.911 Published online by Cambridge University Press

extraction, both in highly idealized cases. It is yet unknown how well these simplified approximations (point absorbers or weak, far-spaced absorbers) describe the performance of periodic WEC arrays consisting of realistic, strong scatterers and absorbers. For example, it is known that trapped waves (also known as Rayleigh–Bloch waves) exist in some periodic systems with fixed bodies, causing large spikes in array response. Rayleigh–Bloch waves were found in periodic arrays of fixed, bottom-mounted cylinders (Maniar & Newman 1997; Evans & Porter 1998) and in similar periodic systems in other branches of physics (e.g. Hsu *et al.* 2013). These trapped waves found for fixed structures (also called 'sloshing' trapped waves) usually cannot be excited when the structure is free to oscillate (McIver 2005; McIver & McIver 2007). Motion-trapped waves, on the other hand, are trapped waves that exist around some freely oscillating bodies, at wavenumbers close to those for sloshing trapped waves. They have been found for isolated three-dimensional bodies (McIver & McIver 2007), but such solutions for a periodic array of freely floating bodies are currently absent. Consequently, it is not yet established whether Rayleigh–Bloch waves exist in periodic WEC arrays where bodies are in motion, or what their effects might be.

We set out to address these questions in this study. Specifically, we uncover Bragg and Laue resonances that occur in periodic arrays of point absorbers and relate them to prominent decreases in array gain (§ 3). An important contribution is the development of a novel multiple-scattering method for periodic arrays of bodies (§ 4, appendix A). This method is then used to study array-related resonances in realistic WEC arrays. For single-body periodic WEC arrays, we perform a systematic analysis of array performance and show that the array gain for body-resonant wavenumbers closely matches that of optimal point-absorber arrays (§ 5). We also find that even a single row of freely oscillating bodies in a periodic array can act as a perfect reflector at particular wavenumbers. For multiple-row rectangular periodic WEC arrays, we find that Bragg and Laue resonances are present at all frequencies, closely resembling the performance of point-absorber arrays (§ 6). We also obtain numerical evidence of the existence of motion-trapped Rayleigh–Bloch waves occurring in energy-extracting or freely oscillating arrays of truncated cylinders, a phenomenon not present in point-absorber arrays. Before addressing these new findings, in § 2 we first outline the description of WEC arrays studied here and give a brief summary of the basic characteristics of general periodic arrays.

2. Overview of periodic (WEC) systems

We consider systems where a sub-array $\mathcal{A}$ of N three-dimensional oscillating, energy-extracting bodies is periodically repeated along one dimension, say in the y-direction, figure 1(a). The spacing between the repeated sub-arrays or, equivalently, the width of a basic cell containing the sub-array, is defined as periodicity d. The spatial configuration $\mathcal{C}$ of a periodic array specifies the positions of the bodies in $\mathcal{A}$ and periodicity d. We use the term 'row' to refer to a subset of the entire array, which consists of only one body from $\mathcal{A}$ periodically repeated. The water depth h is assumed constant. The array interacts with an inviscid, monochromatic plane wave (angular frequency ω, wavenumber k, amplitude A) that propagates at an incident angle θ_I relative to the array normal (x-axis). We consider here the case of small wave steepness ($kA \ll 1$) and small body motion, so the system can be studied in the context of linear potential flow.

The problem is governed by the three-dimensional Laplace equation $\nabla^2\Phi = 0$, where $\Phi(x, y, z)$ is the complex velocity potential (the real-valued velocity potential

https://doi.org/10.1017/jfm.2018.911 Published online by Cambridge University Press

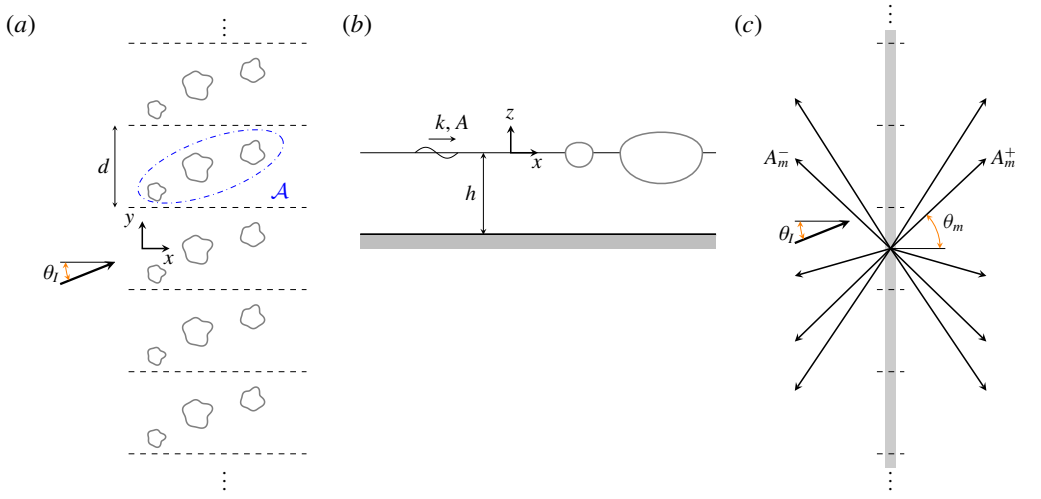

FIGURE 1. (*a*) Top view of the spatial configuration of a periodic array of sub-arrays $\mathcal{A}$ with $N=3$ bodies; periodicity is denoted by d. (*b*) Side view of the problem. (*c*) Scattering mode directions θ_m in the far field. The array is represented by the grey strip.

is $\hat{\Phi}(x, y, z, t) = \mathrm{Re}(\Phi \mathrm{e}^{-\mathrm{i}\omega t})$. The linear dynamic–kinematic boundary on the free surface leads to the dispersion relation $\omega^2 = gk \tanh kh$ (g is the acceleration of gravity). In the open domain, i.e. away from the virtual vertical cylinders containing each body, the depth dependence can be factored out; consequently, the three-dimensional Laplace equation reduces to the two-dimensional Helmholtz equation $\nabla_H^2 \Phi + k^2 \Phi = 0$, where $\boldsymbol{\nabla}_H = (\partial_x, \partial_y)$ is the gradient operator in the horizontal plane.

In addition to the standard boundary conditions on the body surfaces and the bottom ($z=-h$) (Mei, Stiassnie & Yue 2005), the potential Φ satisfies the periodicity condition imposed by the periodicity of the underlying array. This condition is called Bloch theorem (Ashcroft & Mermin 1976), and it states that in a periodic system the values of a field at equivalent locations in two different cells differ only in the phase caused by the incident wave at those locations. For periodic arrays considered here, the Bloch theorem reads

$$\Phi(x, y + d, z) = \mathrm{e}^{\mathrm{i}\beta d} \Phi(x, y, z), \tag{2.1}$$

where $\beta \equiv k \sin\theta_I$. β is the component of the wavevector along the array (also known as the Bloch wavenumber or as the crystal wavevector in solid-state physics).

The periodic nature of the problem requires that only plane waves are present in the far field, and are allowed to propagate in certain directions only. The propagation directions θ_m depend solely on the periodicity d, wavenumber k and the incident angle θ_I and are governed by the grating equation (e.g. Twersky 1956; Falnes & Budal 1982; Maystre 2012)

$$\sin\theta_m = \sin\theta_I + \frac{2\pi}{kd} m, \quad m = 0, \pm 1, \pm 2, \ldots. \tag{2.2}$$

Here, the index m denotes the scattering mode, i.e. a planar wave propagating in direction θ_m with amplitude A_m in the far field. We consider incident waves that are

https://doi.org/10.1017/jfm.2018.911 Published online by Cambridge University Press

propagating from the left half-plane ($-\pi/2 < \theta_I < \pi/2$), so the transmitted waves are plane waves occupying the right half-plane, and the reflected waves the left one. We denote the transmitted wave properties as θ_m^+ and A_m^+, and the reflected wave properties as θ_m^- and A_m^-. Note that $\theta_m^+ \equiv \theta_m$ and $\theta_m^- \equiv \pi - \theta_m$; in particular $\theta_0^+ = \theta_I$ and $\theta_0^- = \pi - \theta_I$ (mirror reflection).

As evident from (2.2), when the value of kd increases past a certain critical value, a new scattering mode appears in the far field. The emergence of, say, the mth mode occurs when $|\sin\theta_m| = 1$, resulting in the critical wavenumber $(kd)_m^{cr}$

$$(kd)_m^{cr} = m\frac{2\pi}{\pm 1 - \sin\theta_I}. \tag{2.3}$$

The new mode emerges at the so-called grazing angle $|\theta_m| = \pi/2$, i.e. it propagates along the grating. A further increase in kd past $(kd)_m^{cr}$ results in aligning θ_m^+ closer to θ_I (or for reflected waves θ_m^- closer to $\pi - \theta_I$). For $\theta_I > 0$, the lowest critical wavenumber occurs for $m = -1$. We denote by $\mathcal{M}$ the set of all indices of the propagating modes in the far field

$$\mathcal{M}(\theta_I, kd) = \left\{ m : \left| \sin\theta_I + \frac{2\pi m}{kd} \right| < 1, m \in \mathbb{Z} \right\}. \tag{2.4}$$

The scattered free surface η_S in the far field can then be written as a superposition of planar waves propagating in directions θ_m:

$$\eta_S^{\pm} = \sum_{m\in\mathcal{M}} A_m^{\pm} \mathrm{e}^{\mathrm{i}kr\cos(\vartheta - \theta_m^{\pm})}, \quad r|\cos\vartheta| \to \infty, \tag{2.5}$$

where (r, ϑ, z) is a cylindrical coordinate system centred at the origin.

When a new scattering mode appears, there is a redistribution of energies (or, equivalently, of amplitudes $|A_m|$) among the existing scattering modes, generally resulting in abrupt changes in the performance. Rayleigh (1907) was the first to derive (2.3) as an attempt to describe the 'anomalies' in the optical diffraction spectrum of a metallic grating that were observed by Wood (1902). Although it was later shown that Rayleigh's theory did not fully explain these Wood anomalies (Maystre 2012), the abrupt changes at $(kd)_m^{cr}$ in periodic systems are called Rayleigh anomalies (Hessel & Oliner 1965). Although not strictly resonances, for terminological convenience, we hereafter refer to these anomalies as Rayleigh resonances, and we call $(kd)_m^{cr}$ (for a given d) the (mth) Rayleigh wavenumber. In general, any kd–θ_I combination for which a scattering mode of any order appears (i.e. for which the condition (2.3) holds) we call the (mth) Rayleigh critical condition. In fluid mechanics, Linton & Thompson (2007) studied the resonant effects at the Rayleigh critical condition caused by an incident acoustic wave on a periodic array of cylinders.

In this study, we focus on the performance of lattice-like configurations of periodic arrays, rectangular-lattice arrays in particular. Here, lattice-like configurations refer to periodic arrays where the bodies are positioned according to the lattice vectors $\boldsymbol{a_1}$ and $\boldsymbol{a_2} = d\hat{\boldsymbol{e}}_y$, with only N bodies in the $\boldsymbol{a_1}$ direction (i.e. N rows). For rectangular-lattice arrays (or rectangular arrays for brevity), $\boldsymbol{a_1} = d_x\hat{\boldsymbol{e}}_x$, where d_x is the row spacing. In addition, we consider arrays consisting of bodies of identical type only. We remark that the multiple-scattering framework presented in § 4 is valid for lattice and non-lattice periodic arrays alike, and possibly composed of different body types.

https://doi.org/10.1017/jfm.2018.911 Published online by Cambridge University Press

In terms of significant wave interaction effects, the prominent physical phenomena occurring in general lattice-like periodic arrays are Bragg and Laue scattering, which are well known in crystallography and solid-state physics (Ashcroft & Mermin 1976). Bragg scattering is the occurrence of a strong reflection due to the constructive interference between the waves reflected from different rows in the lattice. It occurs when the condition (Bragg law)

$$kd_x \cos\theta_I = n\pi, \quad n = 1, 2, \ldots \tag{2.6}$$

is satisfied. In the context of water waves, Bragg scattering effects have been studied for a wide range of problem domains, including periodic bottom ripples (Porter & Porter 2003), periodic arrays of vertical cylinders (Li & Mei 2007*a*) and periodic arrays of horizontal cylinders (Linton 2011). Laue scattering, which is a generalization of Bragg scattering, is the condition when the incident wave and a scattered Rayleigh mode (*m*th one, say) are in such relationship that they are in phase at every lattice point (i.e. at every body). This condition is governed by the Laue equation

$$(\boldsymbol{k} - \boldsymbol{k}_m) \cdot \boldsymbol{a_1} = 2\pi n, \quad n = 1, 2, \ldots, \tag{2.7}$$

where $\boldsymbol{k}$ is the wavevector of the incident wave, and $\boldsymbol{k}_m$ the wavevector of the mth scattered mode.

A striking phenomenon that occurs at isolated wavenumbers in some periodic systems and that is also caused by wave interactions is the presence of embedded Rayleigh–Bloch waves. These waves are the solutions of the homogeneous boundary value problem that do not radiate to the far field, but stay 'trapped' around the array. Usually they are found as modes with frequency below the cutoff frequency for propagation in the far field and as such cannot couple with the incident wave field on a periodic system. (For finite arrays, these Rayleigh–Bloch modes can couple with the incident field, and are often called near-trapped waves as some of their energy 'leaks' away to the far field (e.g. Evans & Porter 1997). This coupling has recently been applied to arrays with slowly varying properties (so-called 'chirped' or 'graded' arrays) to achieve large amplifications of the wave field inside the array for a wide spectrum of incident frequencies (Cebrecos *et al.* 2014; Bennetts, Peter & Craster 2018).) In some rare cases, however, the Rayleigh–Bloch waves for periodic systems are found embedded in the continuous spectrum (Evans & Porter 1998; McIver, Linton & McIver 1998; Linton & McIver 2007) so they can be excited by an incident wave, causing sharp changes in the array response. At the wavenumber kd^{RB} at which an embedded Rayleigh–Bloch wave occurs, the response exhibits a sharp, narrow-banded jump; for wavenumbers away from the jump, the response is unaffected by its presence. The response values are significantly different for wavenumbers just below and above the jump wavenumber. When the response is plotted as a function of wavenumber, this results in an asymmetric response line shape relative to kd^{RB}. These narrow-banded line shapes in the response are also called Fano features or resonances, after Fano (1941) who first discussed them as the (correct) explanation of Wood anomalies (Hessel & Oliner 1965; Maystre 2012).

In WEC arrays, each body is connected to a power take-off (PTO) device, which converts the kinetic energy of the body motion into another, more useful, form. We consider here only linear PTO devices, i.e. those where the power take-off rate b_{PTO} is the constant of proportionality between the device velocity and the force exerted

https://doi.org/10.1017/jfm.2018.911 Published online by Cambridge University Press

by a PTO. For a body j in a WEC array oscillating with a complex amplitude X_j, the mean extracted power P_j (i.e. per one time period) is, thus

$$P_j(\omega) = \tfrac{1}{2}\omega^2 b_{PTO}|X_j|^2. \tag{2.8}$$

The mean extracted power of a periodic array $P_a = \sum_{j=1}^{N} P_j$ (per one cell) is the sum of the mean extracted powers by all the bodies in the sub-array $\mathcal{A}$. The most important quantity describing the performance of WEC arrays is the array gain q, which for a configuration $\mathcal{C}$ with N identical WECs is defined as

$$q(k, \theta_I; \mathcal{C}) = \frac{P_a(k, \theta_I; \mathcal{C})}{NP_{iso}}, \tag{2.9}$$

where P_{iso} is the power extracted by the same WECs operating in isolation. The capture width $W = P_{iso}/P_w$ of a body relates P_{iso} with the power flux $P_w = (1/2)\rho g A^2 c_g$ of the incident wave. An optimal isolated WEC oscillating and extracting energy in heave achieves $kW = 1$ (Evans 1976; Mei *et al.* 2005). The capture width of an array $W_a = P_a/P_w$ is a measure of efficiency of available energy extraction, where $W_a = d\cos\theta_I$ indicates that all incident energy is extracted. In general, the array gain and the array capture width can be defined for arrays of heterogeneous WECs (both in terms of body geometry and extraction characteristics), as well as for directional irregular seas. For simplicity, we focus here only on the array gain for periodic arrays of identical WECs in monochromatic waves.

3. Performance of optimal rectangular-lattice point-absorber arrays

Before considering periodic arrays of general, finite-size WECs, we first consider rectangular periodic arrays with N rows of point absorbers. Although the point-absorber approximation is strictly valid for small bodies ($ka \ll 1$), this assumption simplifies the theoretical treatment and provides a useful foundation for studying periodic WEC arrays of bodies of general shape. The point-absorber theory for periodic arrays was developed by Srokosz (1980), Falnes & Budal (1982) and Falnes (1984). Here, we identify new underlying physical phenomena that were not recognized before, and discuss their effects. These phenomena serve as a basis for comparison with the performance of realistic periodic WEC arrays (in §§ 5 and 6).

For a rectangular periodic array of point absorbers where all the absorbers are heaving with the same amplitude, Falnes & Budal (1982) derived an expression for the optimal gain $\tilde{q}$

$$\tilde{q} = Nkd\left[\sum_{m\in\mathcal{M}} \frac{S_{m,N}}{\cos\theta_m}\right]^{-1}, \tag{3.1}$$

where

$$S_{m,N} = \frac{\sin^2(Nkd_x(\cos\theta_I - \cos\theta_m)/2)}{\sin^2(kd_x(\cos\theta_I - \cos\theta_m)/2)} + \frac{\sin^2(Nkd_x(\cos\theta_I + \cos\theta_m)/2)}{\sin^2(kd_x(\cos\theta_I + \cos\theta_m)/2)}. \tag{3.2}$$

In order to achieve $\tilde{q}$, the phases of motion amplitudes of individual point absorbers are determined from an optimality condition. Since the motion of the point absorbers is constrained to equal amplitudes, $\tilde{q}$ does not represent maximum achievable gain by a periodic array of point absorbers. Nevertheless, the existence of an explicit

https://doi.org/10.1017/jfm.2018.911 Published online by Cambridge University Press

expression for $\tilde{q}$ provides a helpful insight into the phenomena that occur at certain wavenumbers – phenomena that exist in more general cases for which there is no such expression. For $N = 1$, however, the equal-amplitude constraint is no longer relevant, and (3.1) becomes the unconstrained optimal gain. The expression for $N = 1$ was first derived by Srokosz (1980), for $\theta_I = 0°$ only.

We can obtain a general upper limit of gain, i.e. the maximum attainable array gain, by considering the incident energy flux on a general periodic WEC array. The maximum energy that any periodic WEC array can extract is limited by the normal component of the incident energy flux, resulting in the maximum array capture width $(W_a)_{max} = d \cos\theta_I$. Since the array gain can equivalently be expressed as $q = W_a/NW$ and the maximum capture width of a heaving isolated body is $(kW)_{max} = 1$, we obtain the maximum attainable gain q_{max} for an array with N rows

$$q_{max} = \frac{kd}{N} \cos\theta_I, \tag{3.3}$$

relative to the optimal isolated absorbers. This expression is valid for general bodies and general heave amplitudes (if non-heave motion or additional degrees of freedom of motion are considered and $(kW)_{max}$ is increased (e.g. Evans 1976), q_{max} will be proportionally reduced). As such, (3.3) is also valid for the point-absorber arrays studied in this section, and q_{max} can be recognized as the maximum achievable $\tilde{q}$ from (3.1). Since both $S_{m,N}$ and $\cos\theta_m$ are greater than or equal to zero, $\tilde{q}$ is maximum when the denominator is kept to a single ($m = 0$) term. For $m = 0$, (3.2) becomes

$$S_{0,N} = N^2 + \frac{\sin^2(Nkd_x \cos\theta_I)}{\sin^2(kd_x \cos\theta_I)}, \tag{3.4}$$

which results in $q_{max} = \tilde{q}$ for cases when the fraction in (3.4) is zero, i.e. when

$$kd_x \cos\theta_I = \frac{n\pi}{N}, \quad n = 1, \ldots, N-1. \tag{3.5}$$

The expression (3.3) is intuitively understandable – increasing the number of rows N decreases q_{max} as back rows can extract relatively less energy when the front ones are extracting as much as possible. Non-normal incident angles also reduce q_{max}, proportionally to the reduction in the energy flux across the array. An increase in kd, on the other hand, leads to an increase in q_{max} as the performance of an isolated absorber can potentially be significantly improved through favourable wave interactions occurring in arrays. This potential, however, is difficult to attain for most (especially greater) kd values.

Evaluating $\tilde{q}$ for a range of kd values and for specific d_x/d, N and θ_I values reveals that $\tilde{q}$ undergoes significant oscillations, but also possesses some consistent features, figure 2. The complex oscillatory behaviour of $\tilde{q}$ as a function of wavenumber kd increases with kd, d_x/d, and N. At every Rayleigh wavenumber $(kd)_m^{cr}$, $\tilde{q}$ drops abruptly to zero. Mathematically, this follows from the emergence of a new mode at $|\theta_m| = \pi/2$, causing (one of the terms in the sum in) the denominator in (3.1) to become unbounded. For $N > 1$, $\tilde{q} = q_{max}$ for some wavenumbers, in which case all the incident energy is extracted ($W_a = d$). This mostly occurs for wavenumbers below the first Rayleigh wavenumber $(kd)_1^{cr}$ (i.e. (3.5) holds). For larger kd values, $\tilde{q}$ in general does not achieve q_{max}, but the values of $\tilde{q}$ get larger as q_{max} increases. Note that $\tilde{q}$ for single-row arrays never attains q_{max} – it is at most $\tilde{q} = 0.5\, q_{max}$ (for kd below $(kd)_1^{cr}$), confirming that $(W_a/d)_{max} = 0.5$ for a single-row array (Srokosz 1980).

https://doi.org/10.1017/jfm.2018.911 Published online by Cambridge University Press

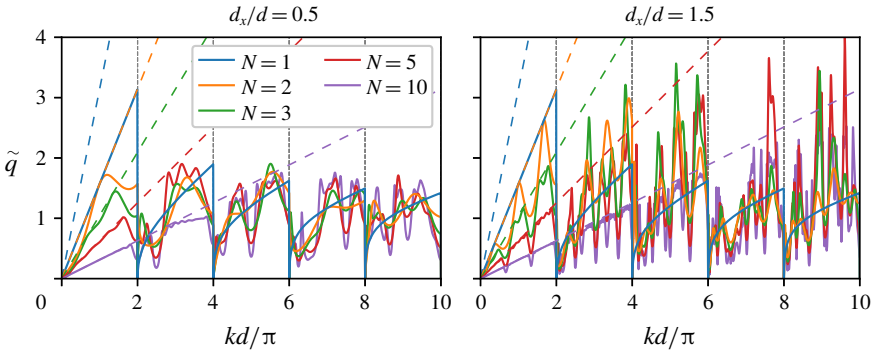

FIGURE 2. Array gain $\tilde{q}$ as a function of kd for $\theta_I = 0°$ for rectangular periodic point-absorber arrays of different aspect ratios d_x/d. The vertical dashed lines at $kd = \text{const.}$ denote Rayleigh critical conditions. The sloped dashed coloured lines denote the maximum achievable gain q_{max}. Note that $\tilde{q}$ for the single-row array ($N = 1$) is unaffected by d_x/d and is shown as a reference in both plots.

We can gain an insight into the complex variation of $\tilde{q}$ with kd by considering the underlying wave interaction mechanisms in periodic arrays. We argue here that there are three important phenomena that lead to a significant reduction in array gain – (i) the aforementioned Rayleigh resonances due to the emergence of new scattering modes; (ii) Bragg resonances occurring for lattice-like arrays of $N > 1$ rows; and (iii) Laue resonances occurring in lattice-like arrays of $N > 1$ rows when one or more scattering modes are present. The first two of these effects were already studied, with some limitations, in the literature, as discussed in § 1. The third phenomenon – Laue resonances – has not been previously discussed in the context of WEC arrays. (A different type of Laue scattering in the context of doubly periodic arrays of bottom-mounted cylinders was studied by Li & Mei 2007*b*.)

We argue that for WEC arrays, Laue interference results in a reduced surface elevation at the bodies, leading to a reduced array gain. The Laue equation (2.7) for rectangular periodic arrays with $\boldsymbol{a_1} = d_x\,\hat{\boldsymbol{e}}_{\boldsymbol{x}}$ becomes

$$kd_x(\cos\theta_I - \cos\theta_m) = 2\pi n, \quad n = 1, 2, \ldots. \tag{3.6}$$

Mathematically, we recognize that (3.6), when approaching the limit, is the condition that would make the first fraction in (3.2) become N^2, thus reducing $\tilde{q}$. We refer to (3.6) (and to (2.7)) as Laue resonance conditions, and label these resonances according to indices (m, n). Note that this is purely an array-configuration-type resonance and is independent of body type and body resonances. The Bragg resonance condition (2.6) can be seen as a special case of Laue equation when $\theta_m = \theta_0^- = \pi - \theta_I$, i.e. when there is strong reflection as a result of interference of the incident and the reflected wave.

To help elucidate the structure of optimal array gain, we plot the contours of $\tilde{q}$ in kd_x–kd space, figure 3. The domain is criss-crossed by well-defined lines along which $\tilde{q}$ is noticeably reduced – these lines represent Rayleigh, Bragg and Laue resonances. Rayleigh wavenumbers $(kd)_m^{cr}$, calculated from (2.3), are the horizontal lines across which there is an abrupt change in $\tilde{q}$ – (cf. figure 2). Bragg resonances are the vertical, equispaced lines, calculated from (2.6), along which there is a reduction in $\tilde{q}$. Laue resonances are the family of curved lines, obtained from (3.6) for each Rayleigh–Bragg (m, n) pair, along which $\tilde{q}$ is also reduced. For a particular

https://doi.org/10.1017/jfm.2018.911 Published online by Cambridge University Press

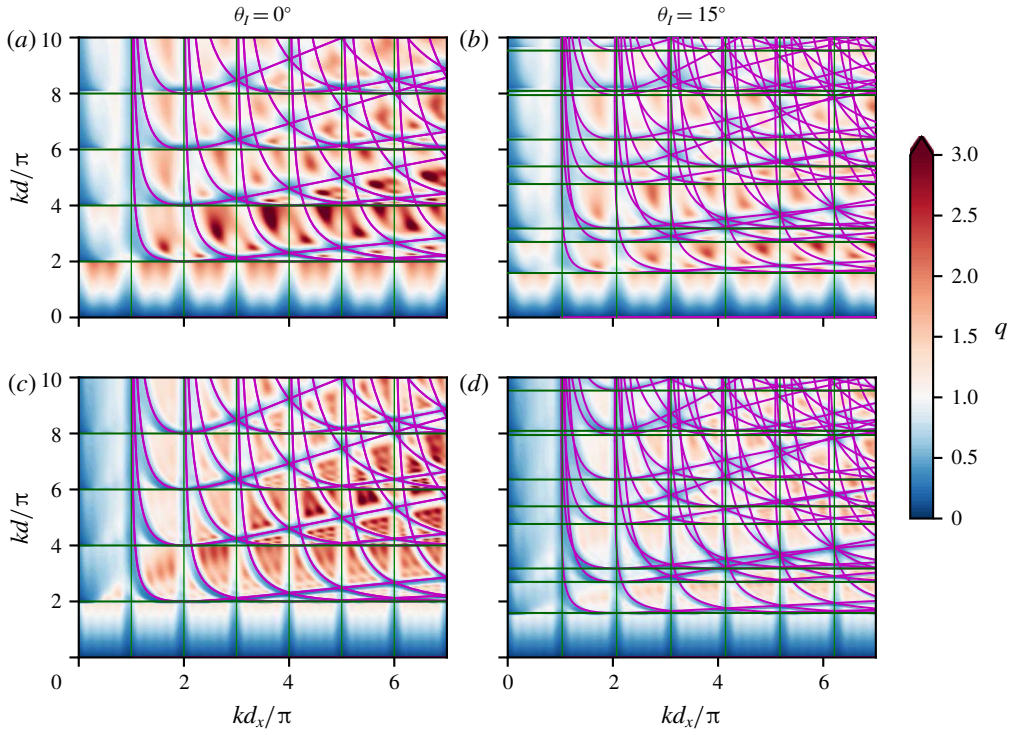

FIGURE 3. Contours of array gain $\tilde{q}$ for rectangular periodic point-absorber arrays of $N = 3$ (a,b) and $N = 5$ (c,d) rows; each column corresponds to one incident angle θ_I. Horizontal green lines represent Rayleigh critical conditions, vertical (grey) lines Bragg resonances and magenta lines Laue resonances. Note that some of the 'high-frequency' oscillations in $\tilde{q}$ (cf. figure 2) are smoothed when plotted as contours due to the limited image resolution.

(m, n)-Laue-resonance curve, the line asymptotes to a vertical for small kd_x. For $\theta_I = 0$, this vertical is the nth Bragg line. For large kd_x, the Laue resonance curve grows monotonically with kd_x. At the intersection with the $2n$th Bragg line, the (m, n) Laue curve is tangent to the mth Rayleigh critical condition line. Where several Laue resonances coincide, the decrease in $\tilde{q}$ is more pronounced – at the particular kd–kd_x value as well as for the values around it. As kd and kd_x are increased, Laue resonances become progressively denser, increasing the portion of the domain where $\tilde{q}$ is significantly reduced (relative to q_{max}). Increasing the number of bodies N in the array decreases the overall $\tilde{q}$, as expected from (3.3), and the troughs in $\tilde{q}$ caused by Bragg and Laue resonances become narrower. Increasing the incident angle θ_I reduces the overall $\tilde{q}$ (in accordance with (3.3)). Furthermore, the non-normal incident angle results in a larger number of distinctive Rayleigh modes, thus increasing the number (i.e. the density) of Laue resonances and, as a result, further reducing $\tilde{q}$ in an increased portion of the domain (relative to normal incidence).

The optimal gain $\tilde{q}$ as a function of kd_x is shown is figure 4, for two incident angles ($\theta_I = 0°$, $15°$) and two kd values. Here, we recognize Bragg resonances as troughs in $\tilde{q}$ at kd_x values given by (2.6). Unlike $\tilde{q}$ at the Rayleigh critical points, $\tilde{q}$ at Bragg resonances exhibits smooth behaviour. For kd below the lowest Rayleigh

https://doi.org/10.1017/jfm.2018.911 Published online by Cambridge University Press

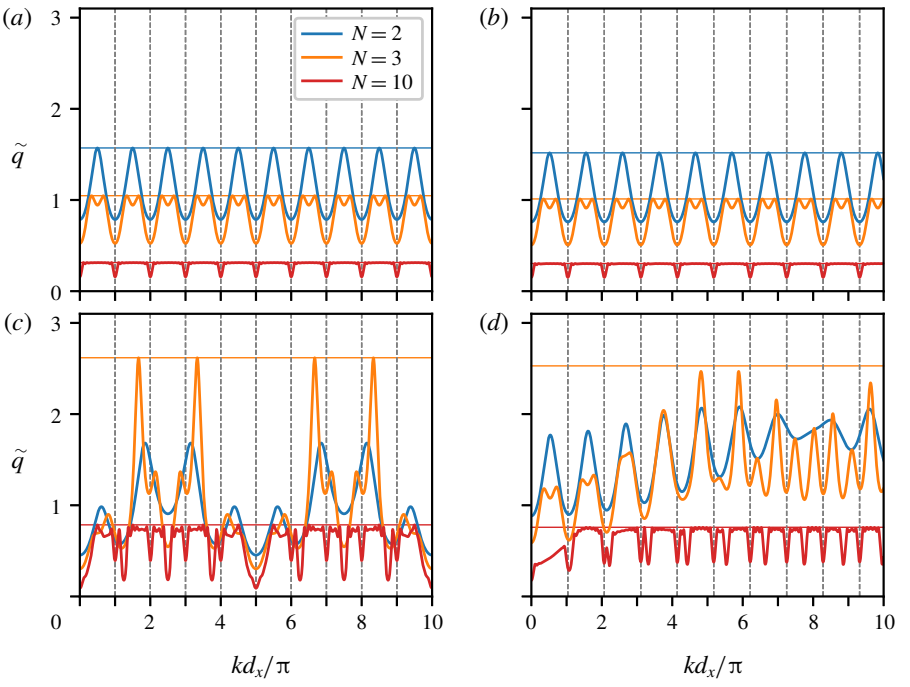

FIGURE 4. Array gain $\tilde{q}$ for rectangular periodic point-absorber arrays of N rows as a function of kd_x, for $kd = \pi$ (*a*,*b*) and $kd = 2.5\pi$ (*c*,*d*) and $\theta_I = 0°$ (*a*,*c*) and $\theta_I = 15°$ (*b*,*d*). Bragg resonances are marked by dashed vertical lines. Thin horizontal lines in corresponding colour mark the maximum attainable gain q_{max} for each N (in (*c*) and (*d*) the q_{max} line for $N = 2$ is outside the presented range).

wavenumber $(kd)^{cr}_{-1}$ (figure 4*a*,*b*), $\tilde{q}$ oscillates between a minimum value $\tilde{q}_{min}$ – which occurs at Bragg resonances (2.6) – and q_{max}. In between Bragg resonances, $\tilde{q}$ achieves $N - 1$ peaks, given by (3.5). We can calculate $\tilde{q}_{min}$ from $S_{0,N}$ by using the Bragg condition (2.6), giving

$$\tilde{q}_{min} = \frac{kd}{2N}\cos\theta_I = \frac{q_{max}}{2}. \tag{3.7}$$

If an additional scattering mode is present (i.e. $kd > (kd)^{cr}_{-1}$), the maximum values of $\tilde{q}$ reach q_{max} only for large values of kd_x (figure 4*c*,*d*). In these cases, deep troughs away from Bragg resonances are the result of Laue resonances. A particularly prominent reduction in $\tilde{q}$ at $kd_x = 5\pi$ in figure 4(*c*) is a result of combined Bragg, and (1, 1)- and (1, 4)-Laue resonances. Bragg resonances are also clearly visible in figure 2 for the $d_x/d = 1.5$, $N > 1$ arrays as two prominent, smooth dips in $\tilde{q}$ for $kd < (kd)^{cr}_{1}$.

Note that troughs at Bragg resonances are pronounced even for a two-row array ($N = 2$), indicating that strong reflection occurs at these conditions. This is different from the Bragg-resonance-related decrease in performance found by Garnaud & Mei (2010), where, because of the weak-absorber assumption, significant effects due to Bragg resonance accumulate only after a large number of rows.

The sharp, abrupt changes in $\tilde{q}$ at Rayleigh wavenumbers are in contrast to the smooth, symmetric behaviour of $\tilde{q}$ around Bragg resonances. However, Rayleigh and Bragg resonances can occur together at the same wavenumber (figure 3), and it is of interest to study how $\tilde{q}$ is affected by these contrasting behaviour patterns. We call

https://doi.org/10.1017/jfm.2018.911 Published online by Cambridge University Press

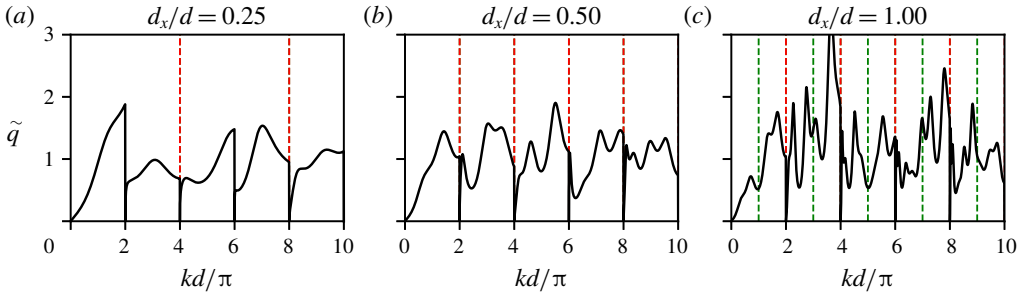

FIGURE 5. Array gain $\tilde{q}$ in the presence of matched Rayleigh–Bragg resonances as a function of kd for three different configurations of rectangular periodic point-absorber arrays with $N = 3$ rows ($\theta_I = 0°$). Rayleigh resonances in these cases always occur every 2π in this figure; matched Rayleigh–Bragg resonances are marked by red vertical lines; isolated Bragg resonances are marked by green vertical lines. Notice that the asymmetry in $\tilde{q}$ for wavenumbers kd just above and below the matched resonances (red lines) is much smaller than that around the isolated Rayleigh resonances.

this condition matched Rayleigh–Bragg resonance, and its existence depends solely on the array configuration d_x/d. For normal incidence, if d_x/d is a rational number, there exist wavenumbers for which the matched Rayleigh–Bragg resonance occurs. Among the set of rational numbers, the arrays with $d_x/d = 1/2$ are special in that Rayleigh and Bragg resonances always occur together, i.e. every occurrence of a Rayleigh resonance is accompanied by a Bragg resonance and *vice versa*. For $d_x/d < 1/2$, there are isolated Rayleigh resonances, and for $d_x/d > 1/2$ there are isolated Bragg resonances. In figure 5, we show $\tilde{q}$ for three-row periodic point-absorber arrays of different configurations d_x/d at normal incidence. We contrast the response at matched Rayleigh–Bragg resonances with that at isolated Rayleigh and Bragg resonances. When a matched Rayleigh–Bragg resonance occurs, $\tilde{q}$ still exhibits a sharp, narrow-banded drop to zero as for an isolated Rayleigh resonance, but $\tilde{q}$ values for wavenumbers below and above the resonance are more similar. As a result, the behaviour of $\tilde{q}$ across the matched Rayleigh–Bragg is smoothed out.

Finally, we remark that the physics behind Laue resonances relies on the lattice-like arrangement of the scatterers in a periodic array, so these resonances should exist in other lattice-like periodic WEC arrays, with similar effects. For example, for an oblique periodic array with the lattice vectors $\boldsymbol{a_1} = (c\ \cos\ \gamma,\ c\ \sin\ \gamma)$, the Laue-resonance condition (2.7) becomes

$$kc(\cos(\theta_I - \gamma) - \cos(\theta_m - \gamma)) = 2\pi n, \quad n = 1, 2, \ldots. \tag{3.8}$$

The skewness of the array lattice in that case would affect the incidence angle at which Laue resonances are most prominent. Furthermore, the equal-amplitude constraint imposed on point-absorber arrays presented in this section is purely for mathematical convenience; we argue here and show in § 6 that the salient phenomena presented here also exist for lattice-like WEC arrays of finite-size bodies in unconstrained motion.

While the point-absorber theory provides a valuable insight into the absorption dynamics of periodic WEC arrays, it is an approximation that neglects several aspects (e.g. diffraction effects, evanescent waves) that are important for practical applications. We present a method that is capable of treating general, realistic WEC arrays next.

https://doi.org/10.1017/jfm.2018.911 Published online by Cambridge University Press

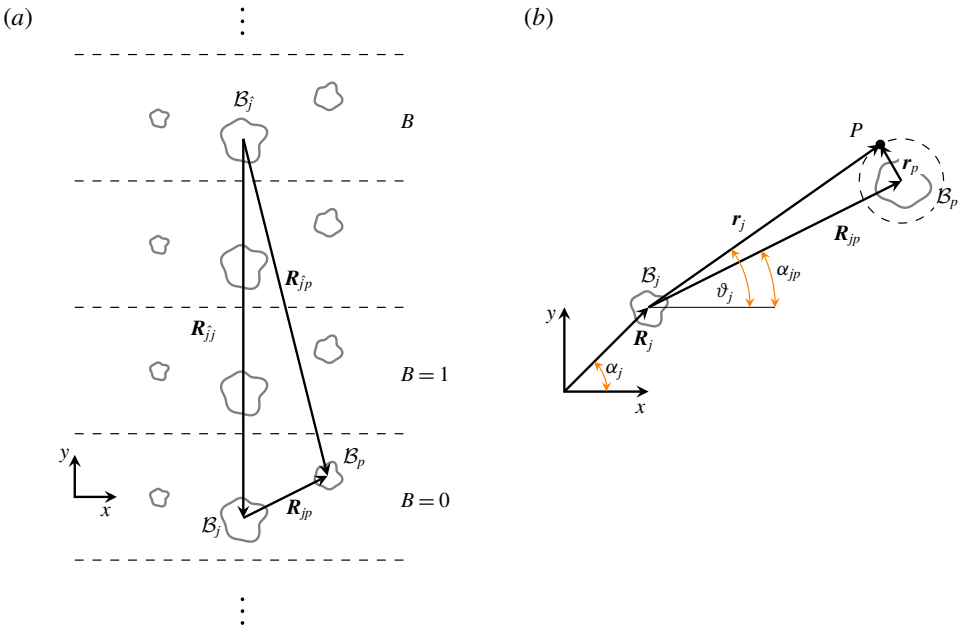

FIGURE 6. (*a*) Infinite array of periodically repeated sub-arrays of scatterers. The decomposition of the distance vector $\boldsymbol{R}_{\hat{j}p}$ between the bodies $\mathcal{B}_{\hat{j}}$ and $\mathcal{B}_p$ into $\boldsymbol{R}_{\hat{j}j}$ and $\boldsymbol{R}_{jp}$ is shown. (*b*) Local coordinate systems of bodies $\mathcal{B}_j$ and $\mathcal{B}_p$.

4. A direct algebraic method for general-shape multi-body periodic arrays

In this section, we present a new multiple-scattering method for periodic arrays consisting of sub-arrays of closely spaced bodies of arbitrary geometry. The approach is based on the Kagemoto & Yue (1986) method for arrays with a finite number of bodies; it generalizes the formulation for a single-body periodic array (Peter *et al.* 2006) and that for periodic rows spaced far apart (Peter & Meylan 2009). It uses only the isolated body hydrodynamic coefficients, without the need for calculating those of the array itself. The method is applicable to fixed, freely oscillating or energy-extracting bodies in any number of degrees of freedom, or a combination thereof. The full formulation is somewhat involved with a number of important intermediate results, and the details are provided in appendix A. For clarity, we highlight below the key steps of the derivation and the main results.

Consider an infinite array formed by a periodically repeating sub-array $\mathcal{A}$ of N bodies along the y-axis with periodicity d, figure 6. The bodies $\mathcal{B}_i$ in the array are spaced far enough so that the virtual vertical cylinders that contain each body do not intersect (i.e. so that the potential outside the cylinders can be expressed in terms of cylindrical harmonics, see (A 4)); the spatial configuration of the sub-array $\mathcal{A}$ is otherwise without constraints. Each of the bodies $\mathcal{B}_i$ in $\mathcal{A}$ can be of an arbitrary shape. The position of body $\mathcal{B}_j$ is given by a vector $\boldsymbol{R}_j = (R_j, \alpha_j)$. A local cylindrical coordinate system $\boldsymbol{r}_j = (r_j, \vartheta_j, z)$ with the origin O_j centred at the body $\mathcal{B}_j$ is defined for each body. The bodies can be fixed, or can be oscillating according to some known equation of motion.

The standard approach in the multiple-scattering framework is to express the total potential as a sum of the incident wave potential and the unknown scattered wave

https://doi.org/10.1017/jfm.2018.911 Published online by Cambridge University Press

potentials (and radiated wave potentials if the bodies are oscillating) for each of the bodies in the array. This can also be expressed relative to a particular body as the total incident potential for that body (consisting of the incident plane-wave potential and the scattered wave potentials of other bodies) and the scattered wave potential of that body alone. In order to determine the unknown potentials, we express the total incident and the scattered wave potential on a particular body in terms of partial waves (with propagating and evanescent radial components, and angular components), which are represented by a number of unknown coefficients that need to be determined. These coefficients can be represented by unknown vectors, say $\boldsymbol{c}^p$ and $\boldsymbol{d}^p$ for the scattered and the incoming wave potential on body $\mathcal{B}_p$, respectively. The goal is to express the incoming and scattered wave potentials on a body in terms of the same coordinate system so that the diffraction boundary condition imposed on that body can be used to determine the relationship between $\boldsymbol{c}^p$ and $\boldsymbol{d}^p$. Since the overall problem is linear, we can express that relationship in a matrix form as

$$\boldsymbol{c}^p = \boldsymbol{T}^p \cdot \boldsymbol{d}^p, \tag{4.1}$$

where $\boldsymbol{T}^p$ is the diffraction transfer matrix or $\boldsymbol{T}$-matrix of body $\mathcal{B}_p$ (Kagemoto & Yue 1986; Martin 2006). The $\boldsymbol{T}$-matrix depends only on the body shape and is independent of the actual wave field around the body, so it can be pre-calculated (analytically or numerically) for a body in isolation. To solve the array problem, we express the unknown part of the incident potential on body $\mathcal{B}_p$ (i.e. the unknown part of $\boldsymbol{d}^p$) in terms of $\boldsymbol{c}^p$ and use (4.1) to close the system.

To express the potentials in terms of the same coordinate system, the standard approach is to use the Graf addition theorem for Bessel functions that result from partial wave decomposition of the potentials. The use of the addition theorem results in an expression that explicitly depends on distance vectors between the bodies; the distance vector $\boldsymbol{R}_{\hat{\jmath}p}$ between bodies $\mathcal{B}_{\hat{\jmath}}$ and $\mathcal{B}_p$ is shown in figure 6(*a*). However, unlike for the case of finite arrays, this approach applied to periodic arrays results in a summation over the infinite number of bodies across the cells. For single-row periodic arrays, Peter *et al.* (2006) expressed the contributions from the infinite number of bodies in the form of rapidly converging lattice sum. For multiple, far-spaced rows, Peter & Meylan (2009) used the far-field transmission and reflection matrices to account for the wave interactions between the rows.

In contrast to those efforts, we consider a general case where multiple rows can be closely spaced. To tackle the summation over the infinite number of bodies while accounting for the exact, near-field interaction between the bodies, we (i) use Bloch theorem (2.1) to transform the partial wave coefficients, (ii) decompose the distance vector $\boldsymbol{R}_{\hat{\jmath}p}$ as in figure 6(*a*) and (iii) use the Graf addition theorem again on the resulting vectors. This approach results in two separate summations. The first one accounts for the interactions among the bodies within a sub-array, and it depends only on the distance vectors $\boldsymbol{R}_{jp}$ between these bodies. The terms can be organized into a separation matrix $\boldsymbol{S}^{jp}$ (matrix elements given by (A 14)), which is identical to that for scattering by a finite, non-periodic array (Kagemoto & Yue 1986). The second summation accounts for the interactions among bodies across different cells, and is expressed in terms of a periodicity matrix $\boldsymbol{Q}^{jp}$ (matrix elements given by (A 18) or (A 20)). The sum over the infinite number of cells in the periodicity matrix is expressed in a rapidly converging form (Linton 1998).

As a result, all the potentials are expressed in the same coordinate system, and we use (4.1) to relate the scattered and incident wave coefficients. Thus, we obtain a linear system for the unknown coefficients of the scattered partial waves

$$(\boldsymbol{I} - \boldsymbol{T}(\boldsymbol{S} + \boldsymbol{Q})^{\mathrm{T}}\boldsymbol{H})\boldsymbol{c} = \boldsymbol{T}\boldsymbol{d}, \tag{4.2}$$

https://doi.org/10.1017/jfm.2018.911 Published online by Cambridge University Press

where $\boldsymbol{c}$, $\boldsymbol{d}$, $\boldsymbol{T}$, $\boldsymbol{S}$, $\boldsymbol{Q}$, $\boldsymbol{H}$ are the global block vectors and matrices representing scattered wave coefficients, incident planar wave coefficients, $\boldsymbol{T}$-matrix, separation matrix, periodicity matrix and radiation transfer matrix, respectively; the superscript $(\cdot)^{\mathrm{T}}$ denotes a matrix transpose. The expression (4.2) has several desirable properties. It is valid for bodies of general shape, not necessarily all equal. The bodies are allowed to be closely spaced, and the evanescent near field is fully taken into account. The bodies can be fixed or freely oscillating, and they can also extract energy.

The periodicity matrix $\boldsymbol{Q}$ is a new addition to the original theory for non-periodic arrays. It depends on the periodicity d of the array and the relative position of bodies in the sub-array $\mathcal{A}$, but not on the properties or the motion of the bodies. For a periodic array with a single body ($N = 1$), $\boldsymbol{Q}$ reduces to the well-known Schlömilch sum ((A 19); Linton 1998; Peter *et al.* 2006). If we set $\boldsymbol{Q} = \boldsymbol{0}$, we recover the linear system for finite arrays (Kagemoto & Yue 1986).

The (global) radiation transfer matrix $\boldsymbol{H}$ is another new component in our multiple-scattering formulation. It contains all the information about the dynamics and the radiation properties of the bodies. A body $\mathcal{B}_p$ is represented by an independent block $\boldsymbol{H}^p$

$$\boldsymbol{H}^p = \boldsymbol{I} + \boldsymbol{c}^{\boldsymbol{R}p} \cdot \boldsymbol{\varpi}^{p\mathrm{T}} \tag{4.3}$$

in the global matrix $\boldsymbol{H}$, where $\boldsymbol{c}^{\boldsymbol{R}p}$ is a known matrix of coefficients of radiated waves for unit oscillation velocity of $\mathcal{B}_p$, and $\boldsymbol{\varpi}^p$ is the velocity transfer matrix. The velocity transfer matrix relates the complex oscillation velocity vector $\boldsymbol{V}^p$ of the body $\mathcal{B}_p$ to the scattered wave coefficients through

$$\boldsymbol{V}^p = \boldsymbol{\varpi}^{p\mathrm{T}} \cdot \boldsymbol{c}^p. \tag{4.4}$$

This matrix is obtained from the equation of motion (A 27) for $\mathcal{B}_p$, which, for multiple degrees-of-freedom motion, can be expressed as

$$\boldsymbol{A}^p(\omega) \cdot \boldsymbol{X}^p = \boldsymbol{F}^p(\omega, \mathcal{C}), \tag{4.5}$$

where $\boldsymbol{A}^p$ is the body dynamics matrix (containing added mass and damping matrices for $\mathcal{B}_p$), $\boldsymbol{X}^p$ the complex motion amplitude and $\boldsymbol{F}^p$ the total diffraction force on $\mathcal{B}_p$. Due to the linearity of wave–body interaction, the diffraction force on a body can be related to the coefficients $\boldsymbol{c}^p$ of the scattered partial waves by

$$\boldsymbol{F}^p = \hat{\boldsymbol{F}}^{p\mathrm{T}} \cdot \boldsymbol{c}^p, \tag{4.6}$$

where $\hat{\boldsymbol{F}}^p$ is the diffraction force transfer matrix of body p, which can be calculated for a body in isolation. By relating the velocity to the motion amplitude $\boldsymbol{X}^p = \mathrm{i}\boldsymbol{V}^p/\omega$ and by using (4.4)–(4.6), we obtain the velocity transfer matrix as

$$\boldsymbol{\varpi}^p = -\mathrm{i}\omega \hat{\boldsymbol{F}}^p \cdot (\boldsymbol{A}^p)^{-1}. \tag{4.7}$$

In this new formulation, only the isolated-body hydrodynamic coefficients (added mass, radiation damping) are required, while their array counterparts are never needed. The diffraction force on a body is dependent on the array configuration, but it is expressed through a configuration-independent transfer matrix $\hat{\boldsymbol{F}}^p$. The body dynamics is, thus, completely included and accounted for in the global system matrix (4.2), and both the hydrodynamics and the body dynamics are essentially solved simultaneously.

https://doi.org/10.1017/jfm.2018.911 Published online by Cambridge University Press

Once the equation (4.2) is solved, the dynamics of any body can be trivially evaluated from (4.4).

For practical computations, we truncate the infinite system (4.2) to a sufficient number of evanescent and angular modes, denoted by M and N_p, respectively. With such truncation, $\boldsymbol{c}^j$ and $\boldsymbol{d}^j$ are of the size $M_t \times 1$, where $M_t \equiv (2N_p + 1) \times (M + 1)$, while $\boldsymbol{T}^j$, $\boldsymbol{S}^{jp}$, $\boldsymbol{Q}^{jp}$ and $\boldsymbol{H}^j$ are of the size $M_t \times M_t$. The degree-of-freedom-dependent matrices $\hat{\boldsymbol{F}}^p$, $\boldsymbol{c}^{\boldsymbol{R}j}$ and $\boldsymbol{\varpi}^j$ are of the size $M_t \times n_{DOF}$, where n_{DOF} is the number of degrees of freedom of the body. The total size of system matrices (i.e. $\boldsymbol{T}$, $\boldsymbol{S}$, $\boldsymbol{Q}$, $\boldsymbol{H}$) is $NM_t \times NM_t$, while the size of the scattered wave coefficient vector $\boldsymbol{c}$ for the entire system is $NM_t \times 1$. The matrices $\boldsymbol{T}$ and $\boldsymbol{H}$ depend only on the isolated-body properties, and can be pre-calculated. If the spatial configuration of the sub-array is changed, only the separation matrix $\boldsymbol{S}$ and the periodicity matrix $\boldsymbol{Q}$ need to be re-evaluated, requiring $O(N^2)$ effort. Since N is usually very small ($N \lesssim 10$), these matrices can be assembled quickly. If the array periodicity is changed, the lattice sums in $\boldsymbol{Q}$ have to be recalculated as well. We note that while the formulation (4.2) is valid for general array/sub-array configurations, the convergence of the sum (A 20) contained in $\boldsymbol{Q}$ deteriorates when the maximum distance between any two bodies in a sub-array becomes greater than the periodicity d (see appendix A).

Once the global system (4.2) is solved, we can also obtain the free-surface elevation as

$$\eta = \eta_I + \eta_S = \eta_I + \frac{\mathrm{i}\omega}{g} \sum_{j=1}^{N} \sum_{B=-\infty}^{\infty} \sum_{n=-\infty}^{\infty} \sum_{m=0}^{\infty} c^j_{mn} P^B \mathrm{K}_n(k_m r_{j,B}) \mathrm{e}^{\mathrm{i}n\vartheta_{j,B}} \psi_m(0), \tag{4.8}$$

where $P_B \equiv \mathrm{e}^{\mathrm{i}Bkd\sin\theta_I}$ is the phase factor for cell B, $\mathrm{K}_n(x)$ is the modified Bessel function of the second kind and the index j, B refers to body j in cell B (see (A 2)). While the expression (4.8) gives a detailed picture of the free-surface elevation around the array, it is not helpful in revealing the far-field structure. We obtain the complex amplitudes A^+_μ and A^-_μ of transmitted and reflected waves in the far field as (details given in § A.2)

$$A^\pm_\mu = \mp \frac{\omega\pi}{g\,kd} \frac{1}{\cos\theta_\mu} \sum_{p=1}^{N} \mathrm{e}^{\mp \mathrm{i}kR_p\cos(\theta_\mu \mp \alpha_p)} \sum_{n=-\infty}^{\infty} (\pm 1)^n \boldsymbol{c}^p_{0n} \mathrm{e}^{\pm \mathrm{i}n\theta_\mu}, \quad \mu \in \mathcal{M}, \tag{4.9}$$

where $\mathcal{M}$ is defined in (2.4). For a single fixed body in the basic cell ($R_p \equiv 0$), the expression (4.9) reduces to the well-known result (Twersky 1962; Peter *et al.* 2006)

$$A^\pm_\mu = \mp \frac{\omega\pi}{g\,kd} \frac{1}{\cos\theta_\mu} \sum_{n=-\infty}^{\infty} (\pm 1)^n c_{0n} \mathrm{e}^{\pm \mathrm{i}n\theta_\mu}, \quad \mu \in \mathcal{M}. \tag{4.10}$$

These complex far-field amplitudes satisfy the energy conservation equation

$$\sum_{\mu\in\mathcal{M}} (|A^+_\mu + \delta_{\mu 0}|^2 - |A^-_\mu|^2) \cos\theta_\mu = \cos\theta_I - \Delta E, \tag{4.11}$$

where $\Delta E = P_a/(1/2)\rho g c_g d$ accounts for the total power P_a extracted by all absorbers (c_g is the group velocity). If no energy is extracted (fixed or freely oscillating bodies), $\Delta E = 0$. This energy conservation check is performed in all our calculations and (4.11) is satisfied to $O(10^{-8})$ at least.

The generality of this method makes it a valuable tool in the analysis of periodic arrays of general bodies. Its computational speed and the ability to calculate the necessary details of overall array performance, as well as the performance of every body in the array, make it a useful tool for the practical design of WEC arrays.

https://doi.org/10.1017/jfm.2018.911 Published online by Cambridge University Press

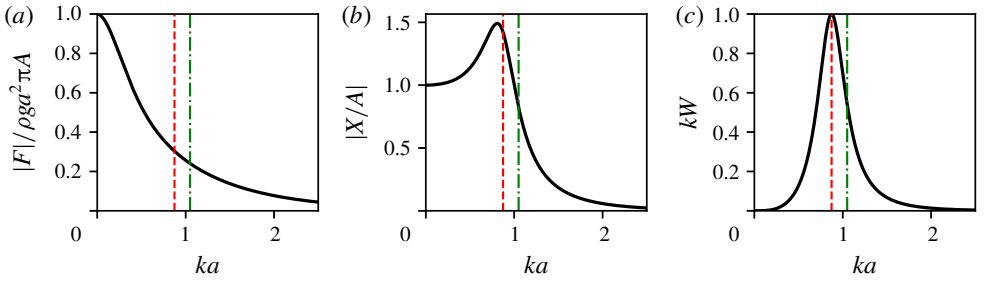

FIGURE 7. Isolated-body performance of a truncated cylinder of radius $a/h = 0.3$ and draft $H/h = 0.2$. (*a*) Non-dimensional amplitude of heave diffraction force (ρ is the fluid density). (*b*) Heave amplitude. (*c*) Non-dimensional capture width kW. Red dashed line marks the resonant wavenumber $k_r a$, green dash-dot line marks the super-resonant wavenumber $k_{sr}a = 1.2k_r a$.

5. Energy extraction by a single-row periodic arrays

In this section, we apply the multiple-scattering method presented in § 4 to the analysis of single-row ($N = 1$) periodic arrays consisting of finite-sized heaving WECs. We study the effects of periodicity d on the array performance in monochromatic waves.

The body geometry we consider here is a truncated vertical cylinder of radius $a/h = 0.3$ and draft $H/h = 0.2$; the body mass equals that of the displaced volume. The body is connected to a linear PTO device with a constant power take-off rate b_{PTO}. For simplicity, we set the value of b_{PTO} to be equal to the body radiation damping at the resonant wavenumber $k_r a$, which results in optimal energy extraction at $k_r a$ (i.e. $kW|_{k_r a} = 1$) when the body operates in isolation (Mei *et al.* 2005). This b_{PTO} value is in general not optimal when a body is a part of an array, but it serves as a good basis for comparison. The $\boldsymbol{T}$-matrix and diffraction force transfer matrix $\hat{\boldsymbol{F}}^j$ for the truncated vertical cylinder are calculated based on the approach by Garrett (1971); the added mass and radiation damping coefficients and the radiated wave coefficient matrix $\boldsymbol{c}^{\boldsymbol{R}}$ are calculated based on the approach by Yeung (1981). The response of this converter when operating in isolation is shown in figure 7, as a function of wavenumber ka. We truncate the partial wave decomposition to $N_p = 5$ and $M = 2$, which give converged results for the analyses presented in this study. In addition to quantities presented in figure 7, array gain q, reflection and transmission coefficients $|A^{\pm}|$ are generally within $O(1\,\%)$.

The dependency of array gain q on the periodicity d and wavenumber is plotted in figure 8. In the $d/2a$–kd space, figure 8(*a*,*b*), the vertical slices (constant $d/2a$) correspond to the performance of a particular array, while the Rayleigh wavenumbers $(kd)_m^{cr}$ are represented by horizontal lines. The calculations are performed for a range of array configurations, from closely spaced configurations ($d/2a = 1.1$) to far-spaced ones ($d/2a = 7$). The performance of arrays for a particular wavenumber ka is obtained by observing the values along a ray emanating from the origin ($ka = \pi/2\,(kd/\pi)/(d/2a)$; the performance is calculated up to $ka = 3.0$). The rays for the body-resonant wavenumber $k_r a$ and the super-resonant wavenumber $k_{sr}a = 1.2k_r a$ are plotted to indicate the bandwidth of significant energy extraction by an isolated body (cf. figure 7*c*). The figure reveals that the troughs of $q = 0$ always occur at Rayleigh wavenumbers $(kd)_m^{cr}$. The overall highest values of q occur for $ka > k_{sr}a$,

https://doi.org/10.1017/jfm.2018.911 Published online by Cambridge University Press

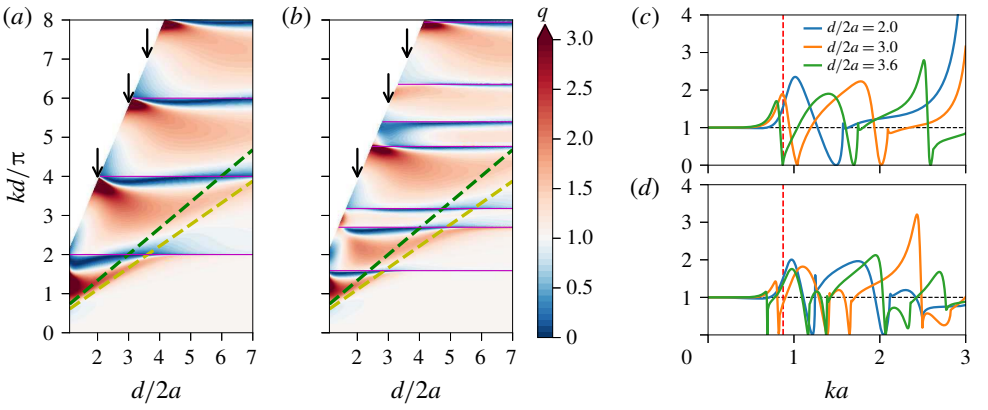

FIGURE 8. (*a*,*b*) Contour plots of array gain q for single-row periodic arrays of truncated vertical cylinders as a function of periodicity $d/2a$ and wavenumber kd, for $\theta_I = 0.0°$ and 15°. The yellow dashed line denotes the body resonant wavenumber $k_r a$; green dashed line the super-resonant wavenumber $k_{sr}a$. The contours are computed for wavenumbers $ka < 3.0$ (cf. figure 7*c*). The contour colour range is cropped to allow for a better resolution at q-values of interest (around 1). The arrows mark the configurations that are plotted in (*c*,*d*). (*c*,*d*) Array gain q for three different configurations ($d/2a = 2.0$, 3.0, 3.6) as a function of wavenumber ka, for two incident angles ($\theta_I = 0°$ and 15°). The red vertical line denotes the resonant wavenumber $k_r a$.

reaching values $q \gtrsim 10$ around $ka \approx 3$ for certain arrays (e.g. for $\theta_I = 0°$, $\max q = 11.3$ at $kd = 3.87\pi$ for $d/2a = 2.02$ array). This indicates that wave interactions in periodic arrays can lead to a significant improvement of otherwise sub-optimal performance of a realistic WEC in the super-resonant regime (figure 7*c*). For wavenumbers ka close to $k_r a$, the maximum value of q is around 2. For $ka < k_r a$, $q \approx 1$, indicating that the array is ineffective in improving the energy extraction in sub-resonant regime over that of an isolated body. The array gain q for three different array configurations ($d/2a = 2.0$, 3.0, 3.6) as a function of wavenumber ka for $\theta_I = 0°$, 15° is shown in figure 8(*c*,*d*). The $d/2a = 3.0$ array attains a (local) gain maximum ($q \approx 1.9$) at body-resonant wavenumber $k_r a$ for $\theta_I = 0°$. For $d/2a = 3.6$, $k_r a$ coincides with the (first) Rayleigh critical condition $(kd)_1^{cr}$, resulting in no energy extraction ($q \approx 0$) at the wavenumber where the body is most efficient at it. For these three configurations, the highest value of $q = 7.93$ occurs for $d/2a = 2.0$ array at $ka = 3.0$ ($kd = 3.82\pi$) and $\theta_I = 0°$. The width of the Rayleigh resonances, i.e. the range around the Rayleigh wavenumber $(kd)_m^{cr}$ where $q \approx 0$, is in general much narrower for $\theta_I = 15°$ than for $\theta_I = 0°$ (e.g. compare the width at the lowest Rayleigh wavenumber for $\theta_I = 0°$ and 15°).

The performance for incident angles $\theta_I = 0°$ and 15° presented in figure 8 provides some indication of how q changes with respect to θ_I. A more detailed picture of that dependency is shown in figure 9 for two different array configurations ($d/2a = 2.0$ and $d/2a = 3.0$), where gain is shown as a function of the wavenumber kd and $\beta d = kd \sin\theta_I$. In this coordinate system, a ray emanating from the origin represents a particular incident angle θ_I, so that the y-axis corresponds to $\theta_I = 0°$, and $y = x$ ray to $\theta_I = 90°$. In the βd–kd plane, the critical values $(kd)_m^{cr}$ are represented by mutually perpendicular families of parallel lines (defined by $\pm(2\pi m - kd \sin\theta_I)$) that intersect the y-axis at (positive) multiples of 2π. (This type of presentation is often

https://doi.org/10.1017/jfm.2018.911 Published online by Cambridge University Press

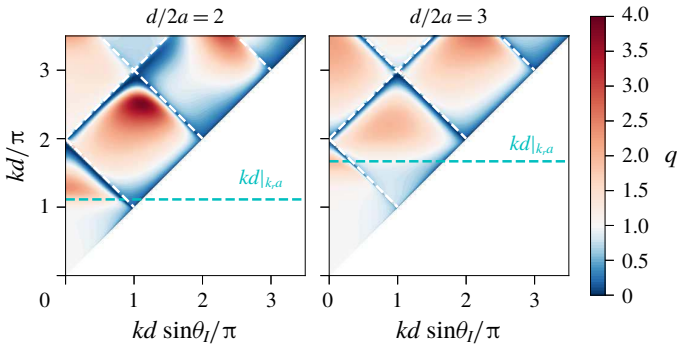

FIGURE 9. Contour plot of array gain q as a function of wavenumbers $kd \sin\theta_I$ and kd, for single-row truncated-vertical-cylinder periodic arrays of periodicity $d/2a = 2.0$ and $d/2a = 3.0$.

used in optics, and it is called light cone because the area above $y = |x|$ lines contains the kd–$kd \sin\theta_I$ values for which light can propagate in free space. This, of course, holds for water waves as well.) The plots show that the high q values are corralled within regions bounded by Rayleigh critical lines $(kd)_m^{cr}$, along which q is zero. The highest values of q within each region are skewed toward larger kd values. Within the plotted range, the highest q value for the $d/2a = 2.0$ array is $\max q = 3.83$, achieved for $\theta_I = 27^\circ$ and $kd = 2.50\pi$.

To gauge how well single-row periodic arrays of truncated vertical cylinders perform at their best, we compare the gain at two particular wavenumbers, $k_r a$ and $k_{sr} a$, with the optimal gain $\tilde{q}$ of single-row periodic point-absorber arrays, figure 10. The performance of a realistic-body periodic array at resonant wavenumber $k_r a$ generally follows that of optimal point absorber for both incident angles. However, q does not attain the same maximal values as $\tilde{q}$ (maximum values at $k_r a$ are 1.94 and 1.72 for $\theta_I = 0^\circ$ and $\theta_I = 15^\circ$, respectively), and q does not exhibit such an abrupt drop to zero as that of $\tilde{q}$. The lower maximum values of q at $k_r a$ are due to the fact that the PTO damping rate b_{PTO} that is optimal for isolated-body operation at $k_r a$ is no longer optimally tuned for maximum extraction in array configuration. We can see the effect of different (constant) values of b_{PTO} on $q(k_r a)$ in figure 11. Lowering b_{PTO} generally brings q closer to the maximum peaks of $\tilde{q}$. However, the optimal b_{PTO} for a WEC array is a function of both the wavenumber ka and the periodicity d because the global (array) radiation damping coefficient is also a function of kd as a result of the wave interaction effects. Tuning b_{PTO} to the optimal value at each wavenumber would bring q closer to $\tilde{q}$.

The body motion at super-resonant wavenumber $k_{sr} a$ is far from being optimal, so the gain $q(k_{sr} d)$ does not follow that of optimal point-absorber arrays, figure 10. Consequently, the configurations (i.e. periodicities) for which $q(k_{sr} d) > \tilde{q}$ do not indicate the configurations of realistic WEC arrays that outperform the optimal point-absorber arrays, but indicate the configurations where array effects can significantly improve otherwise severely sub-optimal performance of an isolated body. For non-normal incidence $\theta_I = 15^\circ$, we again observe that the width of the Rayleigh resonances is narrower than that at $\theta_I = 0^\circ$. Surprisingly, for some configurations that operate above the first Rayleigh critical point, $q(k_r d) > \tilde{q}$, indicating that in this case the truncated-vertical-cylinder array is outperforming the point-absorber array, as the

https://doi.org/10.1017/jfm.2018.911 Published online by Cambridge University Press

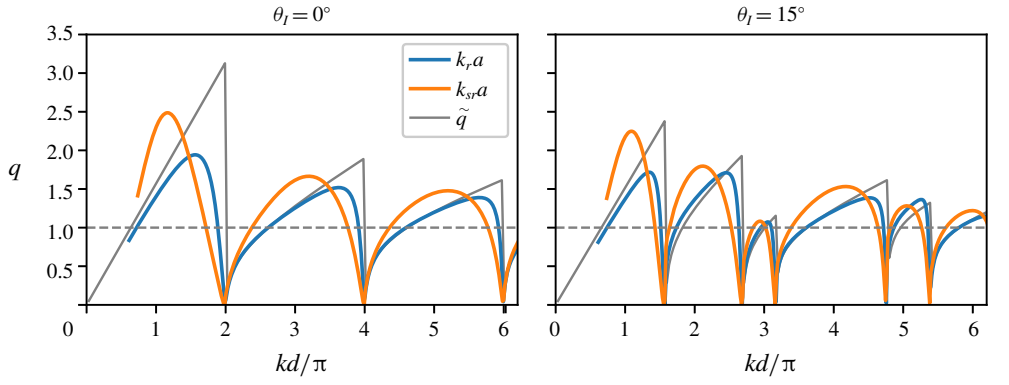

FIGURE 10. Comparison of array gain q of single-row periodic arrays of truncated vertical cylinders for resonant $k_r a$ and super-resonant $k_{sr} a$ wavenumbers with the theoretical prediction for optimal gain $\tilde{q}$ of point absorbers (3.1), as a function of periodicity d. Rayleigh critical conditions occur at vertical jumps in $\tilde{q}$.

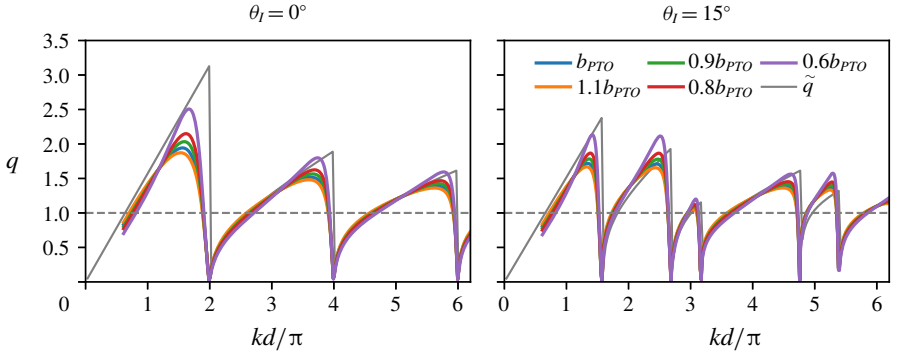

FIGURE 11. Comparison of array gain q at resonant wavenumber $k_r a$ for single-row arrays of truncated vertical cylinders with different (constant) b_{PTO} values, with the theoretical prediction for optimal gain $\tilde{q}$ of point absorbers (3.1) as a function of periodicity d.

isolated performance of both absorbers is equal at $k_r a$. The gain q is still lower than the maximum attainable gain q_{max}, as expected.

The amplitudes of transmission and reflection coefficients $|A_m^{\pm}|$ for $d/2a = 3.0$ array for $\theta_I = 0°$ and $\theta_I = 30°$ are shown in figure 12. We compare the performance of arrays consisting of energy-extracting, freely oscillating or fixed bodies as a function of wavenumber kd. (Note that we plot the combined amplitude $|1 + A_0^+|$ of the incident wave and the zeroth transmitted mode.) In general, when a new mode appears, there are abrupt changes in the amplitudes of other modes, as discussed in § 2. All the variations in mode amplitudes satisfy the energy conservation equation (4.11). The body-resonant wavenumber $k_r d$ is below the first Rayleigh wavenumber $(kd)_1^{cr}$ for normal incidence. For the WEC array at normal incidence, figure 12(*a*), the amplitudes of the modes $|A_0^{\pm}|$ achieve extremes near $k_r d$, which is accompanied by a maximum of array gain q (cf. figure 8*c*). This maximum in q is achieved by extracting a significant energy from both the transmitted A_0^+ and the reflected mode A_0^-, as the comparison with the freely oscillating array shows (figure 12*b*). For non-normal

https://doi.org/10.1017/jfm.2018.911 Published online by Cambridge University Press

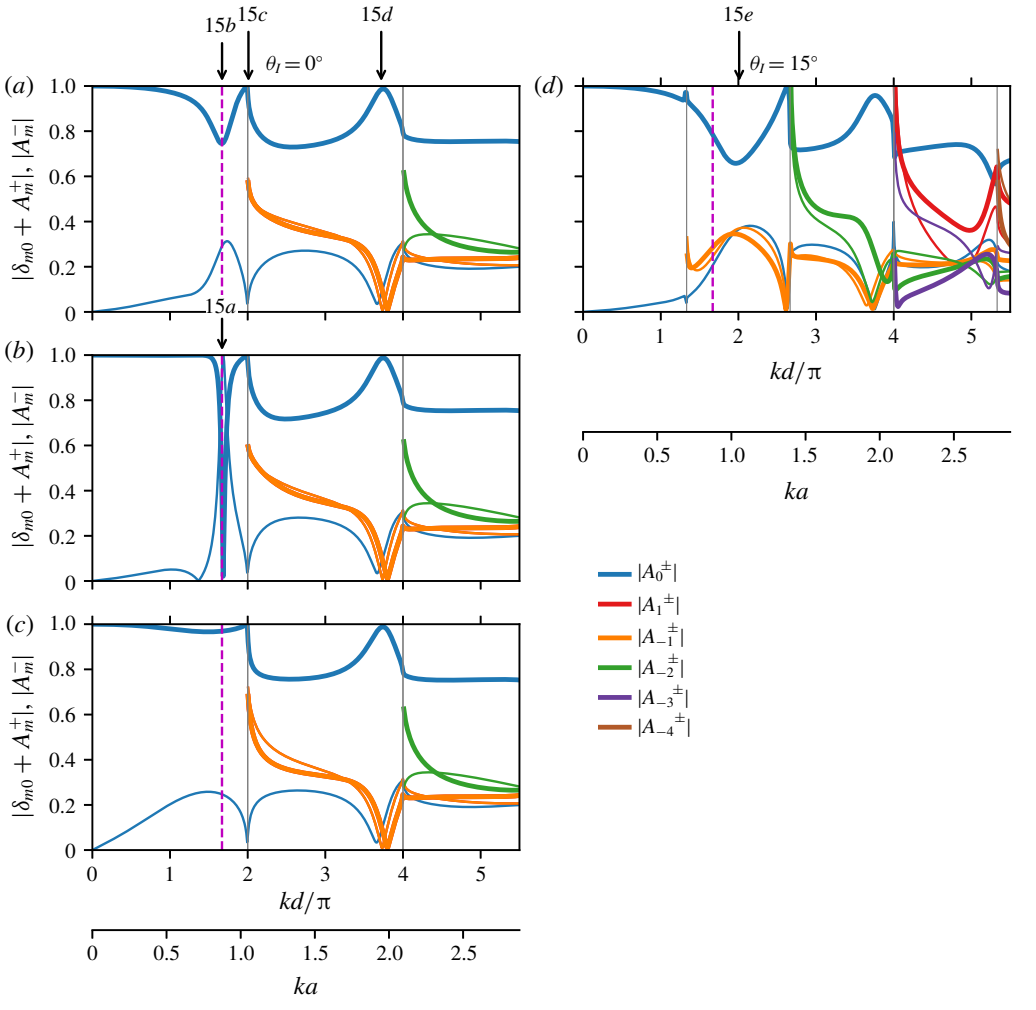

FIGURE 12. Transmission $|\delta_{m0} + A_m^+|$ (thick line) and reflection $|A_m^-|$ (thin line) amplitudes for a single-row truncated-vertical-cylinder periodic array of periodicity $d/2a = 3.0$, for $\theta_I = 0°$, 30° (δ_{m0} is Kronecker delta). (*a*,*d*) Energy-extracting buoys. (*b*) Freely oscillating buoys. (*c*) Fixed buoys. Note that $A_1^\pm$ is hidden below $A_{-1}^\pm$ for $\theta_I = 0°$.

incidence, $k_r d$ falls between $(kd)_1^{cr}$ and $(kd)_2^{cr}$, so there are additional modes present in the far field that radiate energy away from that array (figure 12*d*). None of these modes, however, exhibits an extreme at $k_r d$, and neither does q (not shown). Note that for non-normal incidence the modes are not symmetric with respect to the array normal (x axis), so $A_m^\pm \neq A_{-m}^\pm$ and both are visible in figure 12(*d*). For wavenumbers much larger than $k_r d$, the body motion becomes small (cf. figure 7*b*), so the mode amplitudes are virtually identical between the energy-extracting, freely oscillating and fixed-body arrays. This is true for both normal and non-normal incidence.

It is interesting to note that the freely oscillating array at wavenumber kd_{FR} (close to $k_r d$) behaves as a perfect reflector – the transmitted mode amplitude $|1 + A_0^+|$ drops sharply to zero, and the reflected mode amplitude $|A_0^-|$ becomes one (figure 12*b*). This is solely due to the body motion and not due to some underlying array resonance

https://doi.org/10.1017/jfm.2018.911 Published online by Cambridge University Press

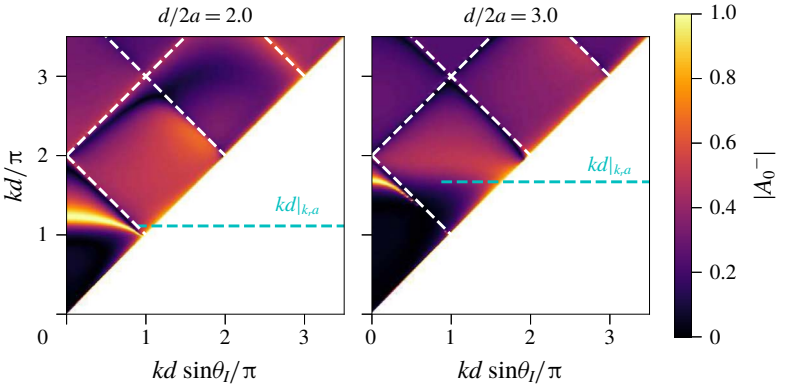

FIGURE 13. Contour plot of the reflected mode amplitude $|A_0^-|$ for a single-row periodic array of freely oscillating truncated vertical cylinders (no energy extraction), as a function of wavenumbers $kd\sin\theta_I$ and kd, for $d/2a = 2.0$ and 3.0.

as the comparison with the periodic array of identical configuration with fixed bodies (figure 12*c* reveals no distinguishable features present around kd_{FR}). For perfect reflection by single-row periodic arrays of heaving bodies, kd_{FR} has to be below $(kd)^{cr}_{-1}$ in order for only one transmitted and reflected mode to be present, figure 13. If more modes are present, the one-degree-of-freedom motion cannot produce the wave field that would simultaneously cancel energy radiation in more than one direction, thus destroying the perfect reflection. The exact value of kd_{FR} depends on periodicity d and the incident angle θ_I, figure 14. The reflected mode amplitude $|A_0^-|$ as a function of d for a given wavenumber $k_r a$ and incident angles $\theta_I = 0°$ and 15° is shown in figure 14(*a*). The amplitude $|A_0^-|$ attains 1 at a single wavenumber kd_{FR}, for both incident angles. For normal incidence, kd_{FR} is only slightly larger than $k_r d$ for the $d/2a = 3.0$ array, as expected from figure 12(*b*). With an increase in θ_I, kd_{FR} is reduced. The dependency of kd_{FR} on d is shown in figure 14(*b*). The kd_{FR} values monotonically increase as a function of $d/2a$ until reaching $(kd)^{cr}_{-1}$ for a given θ_I, beyond which there are no perfect reflections. Correspondingly, ka_{FR} values monotonically decrease from ∼1.2 to ∼0.7. We note that the geometry of this heaving body has not been optimized to achieve the perfect reflection, indicating that this phenomenon is present for more general class of bodies. We confirmed this by conducting numerical simulations (not shown here) on heaving vertical cylinders of different shapes ($a/h = 0.5$, $H/h = 0.1$; $a/h = 0.1$, $H/h = 0.1$) and found that perfect reflection is present at wavenumbers below $(kd)^{cr}_{-1}$ for those geometries as well.

The free-surface amplitude $|\eta|$ for the $d/2a = 3.0$ array at specific wavenumbers and incident angles (marked in figure 12) is shown in figure 15. The effect of perfect reflection is demonstrated in figure 15(*a*), where freely oscillating bodies at body-resonant wavenumber $k_r a$ exhibit large heaving motion and almost completely reduce the free-surface amplitude behind the array ($|\eta| \approx 0$). In front, $|\eta|$ is modulated with an increased amplitude between the nodes, as required by energy conservation. When energy extraction is present at the same wavenumber, figure 15(*b*), the bodies still perform large motions (significant energy extraction), but the array no longer acts like a perfect reflector ($|\eta| > 0$ behind the array). At a wavenumber just above $(kd)^{cr}_{1}$, figure 15(*c*), a new mode of relatively large amplitude has just emerged and is propagating almost perpendicular to the incident wave, causing a significant

https://doi.org/10.1017/jfm.2018.911 Published online by Cambridge University Press

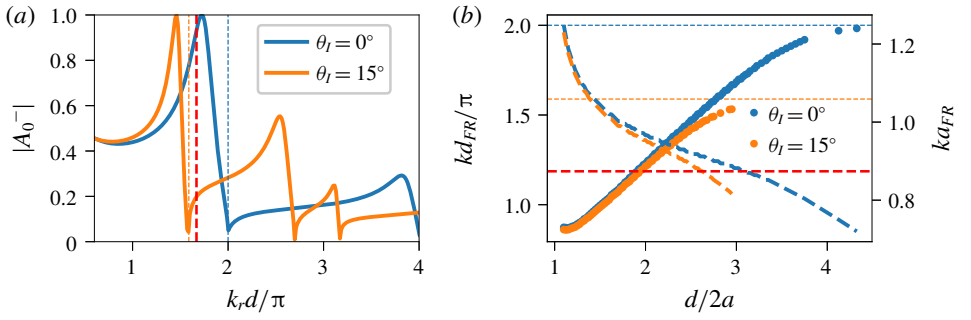

FIGURE 14. (*a*) The reflected mode amplitude $|A_0^-|$ for two different incident angles as a function of periodicity d (at body-resonant wavenumber $k_r a$). Thin vertical dashed lines mark corresponding $(kd)_{-1}^{cr}$; thick vertical dashed red line marks $d/2a = 3.0$ array. (*b*) Wavenumber kd_{FR} (left y-axis, dots) and ka_{FR} (right y-axis, dashed line) at which full reflection occurs as a function of spacing d, for two different incident angles. Horizontal lines in matching colour mark corresponding $(kd)_{-1}^{cr}$; thick red dashed horizontal line marks $k_r a$.

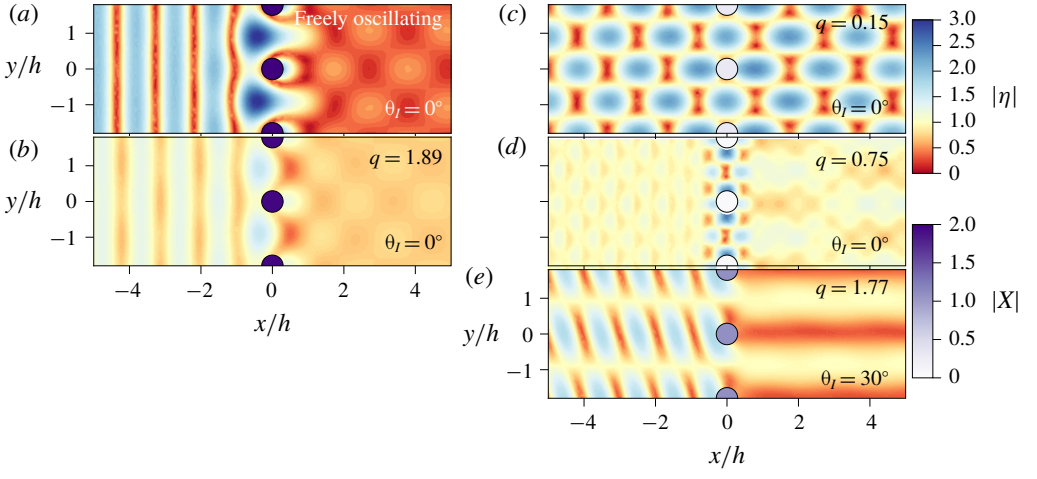

FIGURE 15. Free-surface amplitude $|\eta|$ contours for a single-body periodic array of truncated vertical cylinders of periodicity $d/2a = 3.0$. Waves are incident from the left. (*a*) $kd = 1.67\pi$ ($ka = k_r a$), freely oscillating. (*b*) $kd = 1.67\pi$ ($ka = k_r a$). (*c*) $kd = 2.01\pi$ ($ka = 1.05$). (*d*) $kd = 3.72\pi$ ($ka = 1.95$). (*e*) $kd = 2.01\pi$ ($ka = 1.05$). The body colour corresponds to the heave amplitude (lower colour bar).

modulation of the surface amplitude. The bodies are located in the low value troughs of the free-surface amplitude, resulting in almost zero $|X|$ and q. At $kd = 3.72\pi$, figure 15(*d*), which is still between $(kd)_1^{cr}$ and $(kd)_2^{cr}$, $|1 + A_0^+| \approx 1$ and the rest of the modes are almost zero (cf. figure 12), so the array minimally disturbs the free surface in the far field. Close to the array, however, the surface modulation is significant. The body motion amplitude $|X|$ in figure 15(*c*,*d*) is small, but for different reasons. In figure 15(*c*), the small $|X|$ is caused by a Rayleigh resonance, and it would be significantly larger if the wavenumber were slightly different. In figure 15(*d*), on the other hand, the small $|X|$ is caused by the fact that the wavenumber ka is much

https://doi.org/10.1017/jfm.2018.911 Published online by Cambridge University Press

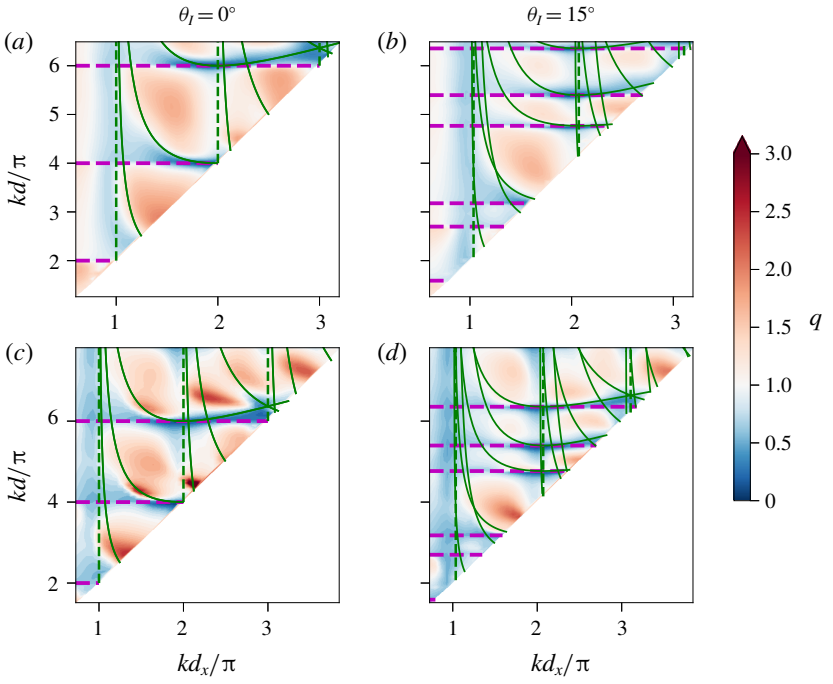

FIGURE 16. Array gain q for a three-row periodic array of truncated vertical cylinders at resonant wavenumber $k_r a$ (a,b) and super-resonant wavenumber $k_{sr} a$ (c,d) as a function of row spacing d_x and periodicity d. Each column corresponds to one incident angle θ_I. Only the values for array configurations that satisfy the domain constraint $(N-1)d_x \leqslant d$ are plotted. Bragg resonances are marked by green vertical dashed lines; Rayleigh critical conditions are marked by magenta horizontal dashed lines. For comparison, point-absorber Laue-resonance lines based on (3.6) are marked by thin green lines.

larger than $k_r a$, so the isolated-body amplitude is very small to start with and a small variation in ka would not change $|X|$ significantly. For a non-normal incidence ($\theta_I = 30°$) case, figure 15(*e*), the bodies exhibit large motion amplitudes, corresponding to large energy extraction ($q = 1.77$). The wide bands of nearly zero amplitude behind the array are a good indication of that.

6. Energy extraction by multi-row periodic arrays

One of the advantages of the multiple-scattering method presented in § 4 is that it is applicable to periodic WEC arrays of closely spaced sub-arrays of general, not necessarily identical bodies. We apply the method here to study the effect of the periodicity d and row spacing d_x on the array performance of rectangular periodic arrays with $N = 3$ rows. For simplicity, we focus on arrays of identical truncated vertical cylinders, having the same shape and PTO characteristic as in § 5; the extraction rate b_{PTO} is kept constant and equal for all the bodies in the array. This choice of b_{PTO} values provides for an insightful study of the phenomena occurring in general (not just optimal) WEC arrays, with a simply defined b_{PTO} distribution.

The array gain q as a function of periodicity d and row spacing d_x for resonant and super-resonant wavenumbers ($k_r a$, $k_{sr} a$) and two incident angles ($\theta_I = 0°$, $15°$) is shown in figure 16. To avoid the slow convergence of the periodicity matrix $\boldsymbol{Q}$

https://doi.org/10.1017/jfm.2018.911 Published online by Cambridge University Press

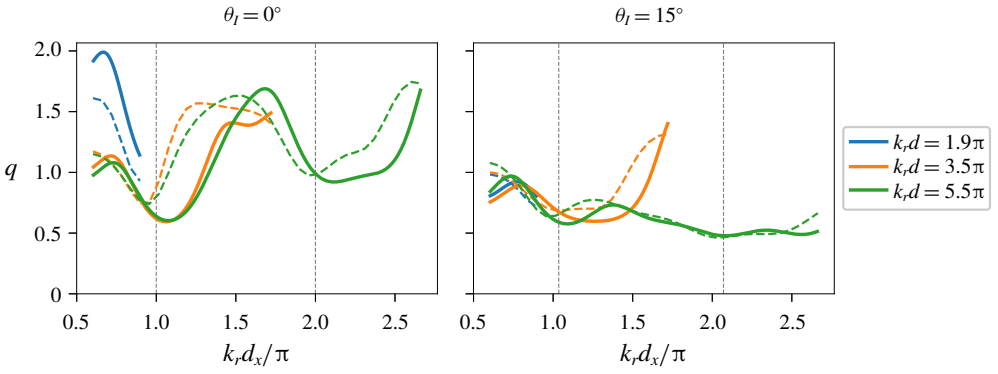

FIGURE 17. Comparison of array gain q for three-row truncated-cylinder periodic WEC arrays at resonance wavenumber $k_r a$ (dashed lines) with array gain $\tilde{q}$ for point-absorber arrays of equivalent configuration in equal-amplitude motion (solid lines), as a function of row spacing d_x. The results are plotted only for the range where the domain constraint $(N-1)d_x \leqslant d$ is satisfied. Vertical dashed lines denote Bragg resonances.

discussed in § 4, we consider here only array configurations that satisfy the domain constraint $(N-1)d_x \leqslant d$. The overall structure of q resembles that of $\tilde{q}$ (cf. figure 3). The decrease in q due to Rayleigh resonances and Bragg resonances are present at all wavenumbers and incident angles, confirming that these phenomena are an inherent feature of lattice-like periodic WEC systems, and not only of the point-absorber ones. Laue-resonance lines for the finite-body periodic arrays are, in general, slightly perturbed from those given by (3.6) due to the small phase shifts in the scattered modes relative to those for point-absorber arrays. For the sake of comparison with the point-absorber arrays, we plot the Laue resonance lines based on (3.6). We find that the regions of lower q in general align well with the point-absorber Laue-resonance lines; the instances where these Laue-resonance lines cross the areas of high q indicate that a larger phase shift in the scattered modes is present. The decrease in q due to Laue resonances is more obvious for larger wavenumbers ($k_{sr}a$) where Laue resonances are denser. Overall, q obtains maximum values of 1.98 and 3.72 at $\theta_I = 0°$ for $k_r a$ and $k_{sr}a$, respectively, and 1.66 and 2.28 for $\theta_I = 15°$. Further increases in q would be possible if the PTOs in a given array configuration were optimally tuned (cf. figure 11) for a specific wavenumber ($k_r a$ or any other). In that case, b_{PTO} of each body in the sub-array would have a different optimal value in general.

The comparison of the array gain q at the body-resonant wavenumber $k_r a$ with the array gain $\tilde{q}$ for point-absorber arrays of equivalent configuration in equal-amplitude motion as a function of row spacing d_x is shown in figure 17. Despite the absence of the equal-motion constraint for the truncated-cylinder WEC arrays, q at $k_r a$ in general follows the behaviour of $\tilde{q}$, but it is even greater than $\tilde{q}$ within some intervals. The high values of q in this case are not a result of the sub-optimal performance of the isolated body (extracted power by an isolated body at resonance is equivalent to that of an optimal point absorber), but are gains caused directly by favourable array interactions. The intervals where $q > \tilde{q}$ indicate the configurations for which the equal-amplitude motion of periodic point-absorber arrays is clearly sub-optimal because periodic arrays of non-optimized WECs (in terms of b_{PTO}, shape) are performing better than the point-absorber arrays of identical configuration.

https://doi.org/10.1017/jfm.2018.911 Published online by Cambridge University Press

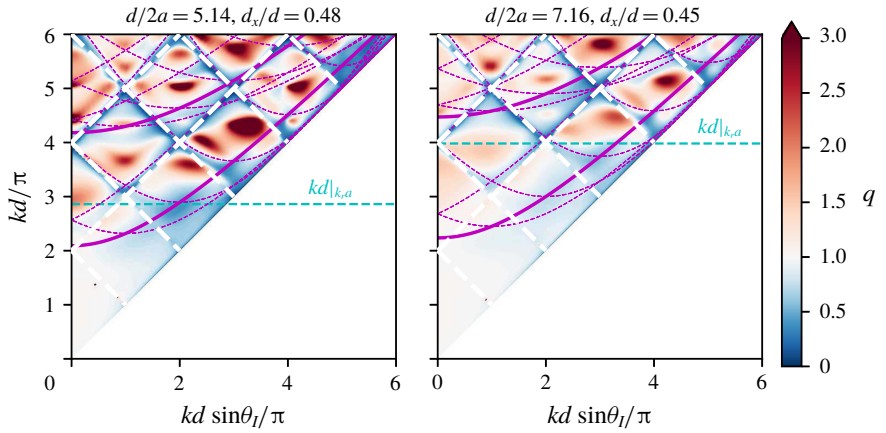

FIGURE 18. Light-cone plot of array gain q for two different three-row periodic arrays of truncated vertical cylinders. Rayleigh critical conditions marked by dashed white lines, Bragg resonances by thick magenta lines, Laue resonances based on (3.6) by thin, dashed magenta lines and the body-resonant wavenumber by a dashed horizontal cyan line.

The light-cone plot of q for two different array configurations, figure 18, reveals the detailed dependence of q on kd and θ_I. The overall structure resembles that of an isolated body (cf. figure 9), with additional troughs in q due to Bragg and Laue resonances. The Laue-resonance lines for point-absorber arrays (i.e. based on (3.6)) are plotted for comparison. Away from Bragg and Laue resonances high gains are attainable, especially for super-resonant wavenumbers (e.g. for $\theta_I = 24°$, $\max q = 6.08$ at $kd = 5.03\pi$; for $\theta_I = 47°$, $\max q = 5.98$ at $kd = 4.34\pi$).

The array gain q for a range of wavenumbers and periodicities in arrays of two different aspect ratios $d_x/d = 0.45,\ 0.495$, is plotted in figure 19. For aspect ratios $d_x/d \lesssim 0.5$, the structure of q is similar to that of $d_x/d = 0.45$. Compared to single-row performance (figure 8), q still preserves the band-like structure determined by Rayleigh wavenumbers, but it is more intricate due to the presence of Bragg and Laue resonances. Higher values of q still occur for larger ka values (e.g. for $d_x/d = 0.45$ configurations at $\theta_I = 0°$, $\max q = 8.60$ occurs for $d/2a = 4.85$ and $kd = 8.50\pi$ ($ka = 2.75$)). For $ka < k_r a$, $q \approx 1$, which indicates that limited gains, in general, are possible in the sub-resonant regime; this behaviour is also similar to that found in single-row periodic arrays (cf. figure 8).

For configurations with the $d_x/d \approx 0.5$ aspect ratio, however, we find new features that cannot be attributed to the Rayleigh, Bragg or Laue resonances identified so far. These new features appear as sharp increases in q that intersect the constant-wavenumber lines at an oblique angle. Consequently, they appear as narrow-banded features in the kd-space for a given array configuration. These are, in fact, Fano features we discussed in § 2 and are the signatures of Rayleigh–Bloch waves. The striking feature of these Rayleigh–Bloch waves is that they are excited by the incident wave, i.e. they are embedded in the continuous spectrum, and their effect is easily recognizable in the response. Since these waves appear in a system where bodies are inherently moving, we borrow the terminology from McIver & McIver (2007) and refer to them as motion-trapped Rayleigh–Bloch waves. Note that these Rayleigh–Bloch waves are absent in the response of point-absorber arrays studied in § 3, including for the array configurations identical to those represented in

https://doi.org/10.1017/jfm.2018.911 Published online by Cambridge University Press

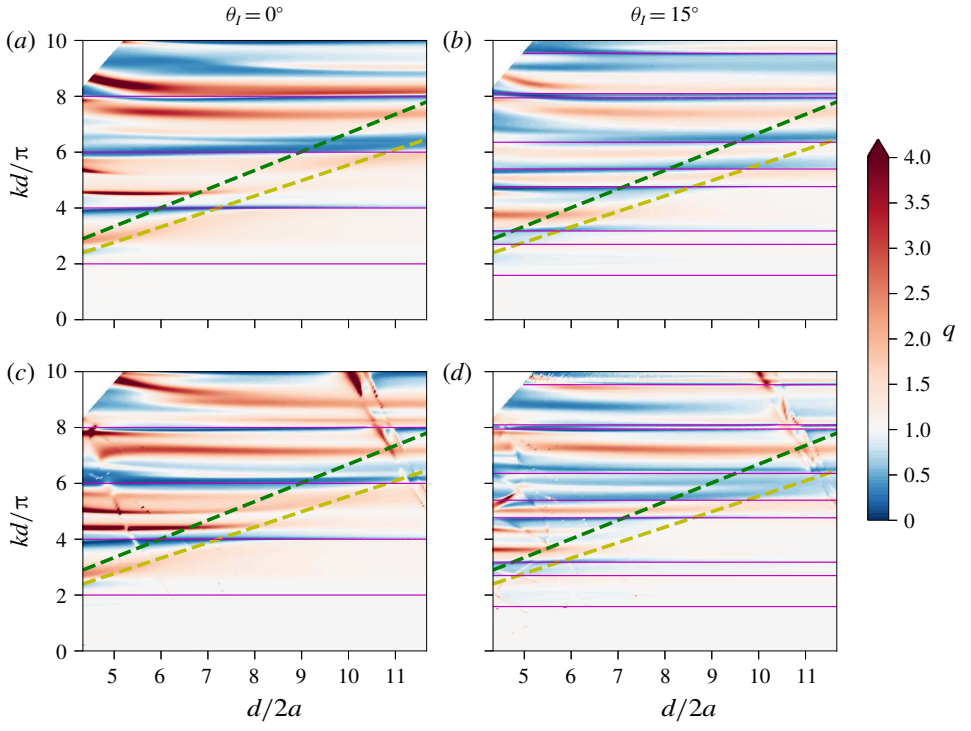

FIGURE 19. Contour plot of array gain q of a three-row truncated-vertical-cylinder periodic array with aspect ratios $d_x/d = 0.45$ (a,b) and $d_x/d = 0.495$ (c,d). The yellow dashed line denotes the body-resonant wavenumber $k_r a$; green dashed line the super-resonant wavenumber $k_{sr}a$. The contours are computed for wavenumbers $ka < 3.0$ (cf. figure 7*c*). The contour colour range is cropped to allow for a better resolution at q-values of interest (around 1).

figure 19. This stems from the fact that the phenomenon of Rayleigh–Bloch waves is inherently related to finite-size bodies and their interaction with the wave field.

In order to study the structure and the sensitivity of the Rayleigh–Bloch waves, in the following we focus on three periodic arrays that appear to support Rayleigh–Bloch waves, but of slightly different configurations: configuration I with periodicity $d/2a = 5.14$ and row spacing $d_x/d = 0.48$, configuration II with $d/2a = 5.19$ and $d_x/d = 0.50$ and configuration III with $d/2a = 5.20$ and $d_x/d = 0.50$. The minor differences in periodicity and row spacing between these configurations provide a good basis for the sensitivity analysis of trapped waves with respect to configuration perturbations.

The array gain q for configurations I, II and III as functions of wavenumber kd are shown in figure 20. While all three configurations exhibit very similar behaviour for the most of the kd range for $\theta_I = 0°$, figure 20(*a*), configurations II and III exhibit sharp, narrow-bandwidth spikes – Fano features – at distinct wavenumbers kd^{RB}. Both configurations exhibit two Fano features in the plotted interval, one occurring at kd^{RB} below the Rayleigh wavelength $(kd)_1^{cr}$, and one just above it. The first wavenumbers kd^{RB} at which Rayleigh–Bloch waves occur are noticeably different between the two configurations, as are the magnitudes of Fano features, which indicates high sensitivity to perturbations in periodicity. Note that the orientations of the two Fano features for configuration II are different – the first exhibits a small decrease in q followed by a

https://doi.org/10.1017/jfm.2018.911 Published online by Cambridge University Press

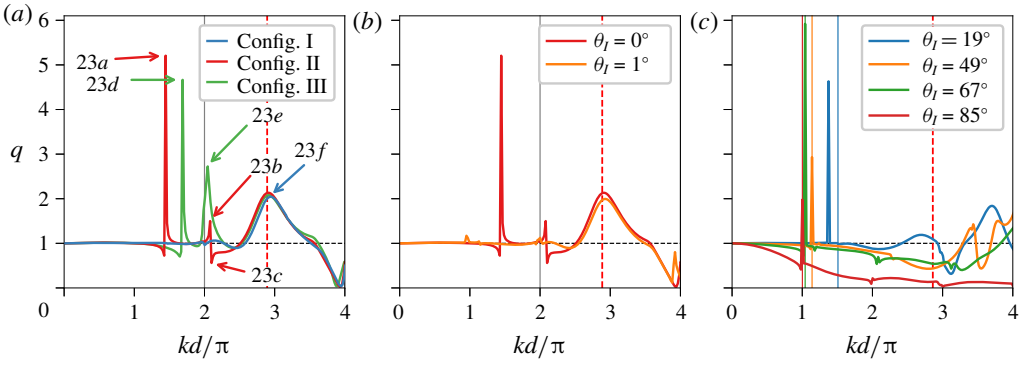

FIGURE 20. Array gain q as a function of wavenumber kd for three-row periodic arrays of truncated vertical cylinders. (*a*) Three different array configurations at $\theta_I = 0°$; (*b*) configuration II at $\theta_I = 0°$, 1°; (*c*) non-normal incidence for configuration I. Rayleigh wavenumbers $(kd)^{cr}_{-1}$ are marked by thin vertical lines (in corresponding colour in (*c*)); the body-resonant wavenumber is marked in dashed red vertical line. Arrows in (*a*) mark the cases that are plotted in figure 23.

sharp jump, while the second is preceded by an increase in q followed by a sharp drop. Comparison of q for configuration II at $\theta_I = 0°$ and $\theta_I = 1°$, figure 20(*b*), reveals that the presence of Rayleigh–Bloch waves is very sensitive to angular perturbations. While for the most of the plotted kd range the two lines are virtually indistinguishable, $q(\theta_I = 1°)$ exhibits no significant Fano features despite only a minor variation in incident angle. Rayleigh–Bloch waves are not limited to normal incidence, however. Array gain q for configuration I at specific non-normal incidence angles is shown in figure 20(*c*). Fano features below the lowest Rayleigh wavenumber $(kd)^{cr}_{-1}$ are present for all plotted incident angles. In the same way as in figure 20(*b*), a slight variation in θ_I will destroy the Rayleigh–Bloch waves.

While the presence of embedded Rayleigh–Bloch waves is highly sensitive to perturbations of k and θ_I, based on figure 19 we can argue that a large range of three-body rectangular periodic arrays with $d_x/d \approx 0.5$ support one or more embedded Rayleigh–Bloch waves at some kd and θ_I. Changing the periodicity (while keeping the same aspect ratio d_x/d) merely changes k and θ_I at which Rayleigh–Bloch waves occur.

The effect of trapped waves on power extraction effectiveness of each body – the percentage of power $p_i = P_i/P_a$ extracted by body i – is shown in figure 21. For configuration I, all the bodies are almost equally effective in energy extraction for wavenumbers below the first Rayleigh wavenumber. Above the first Rayleigh wavenumber, such balance is no longer present and the variation of p_i with kd is different for each body, usually with all three bodies extracting different amounts of energy. At the resonant wavenumber $k_r a$, all the values of p_i are again almost equal. For configuration II, on the other hand, the sharp Fano features are present again – p_i at trapped-wave wavenumbers exhibits an abrupt increase or decrease, and it is most prominent for bodies 1 and 2. Note that the Fano features are also observed in the motion response (not shown). The heave amplitude $|X_i|$ of each body can be calculated from (2.8) and (2.9) as $|X_i| = |X|\sqrt{Nqp_i}$, where $|X|$ is the heave amplitude of an isolated body, figure 7(*b*).

Comparison of the amplitudes of the zeroth scattering modes $|A_0^{\pm}|$ for the three configurations is shown in figure 22. At the first trapped-wave wavenumber kd^{RB}, $|A_0^{+}|$

https://doi.org/10.1017/jfm.2018.911 Published online by Cambridge University Press

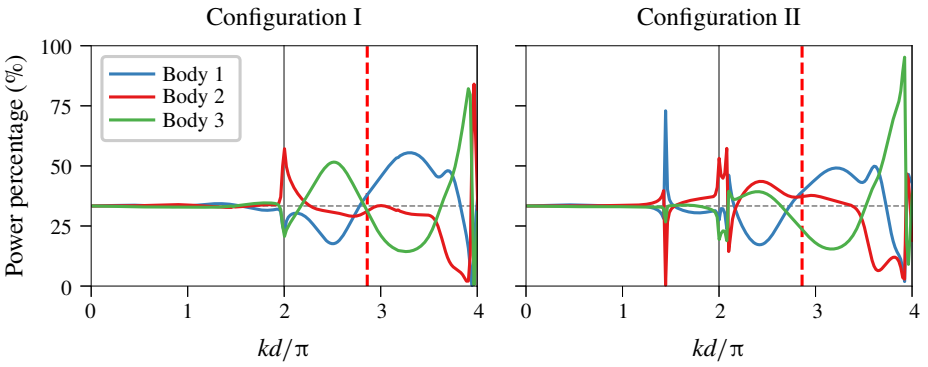

FIGURE 21. Comparison of the percentage of extracted power p_i by each of the bodies in a three-row periodic array of truncated vertical cylinders, for two different array configurations at $\theta_I = 0°$. Rayleigh wavenumbers are marked by grey vertical lines; the body-resonant wavenumber is marked by dashed red vertical lines.

for configurations II and III exhibits a sharp decrease, matched by an equally sharp increase in $|A_0^-|$, as required for energy conservation. The Fano features at the second trapped wavenumber are somewhat less pronounced. Interestingly, the Fano features persist even for same-configuration arrays of freely oscillating bodies (no power extraction) and of fixed bodies, although they are less pronounced in the latter case. This indicates that WEC arrays that support motion-trapped Rayleigh–Bloch waves also support trapped waves in arrays of fixed bodies at the same, or nearly the same, wavenumbers. The trapped waves that occur in fixed structures are called sloshing trapped waves; they have been observed, for example, in isolated three-dimensional bodies with a central moonpool (McIver & McIver 2007).

Note that Fano features in $|A_0^{\pm}|$ for these three-row periodic arrays are different from the narrow-banded, total reflection features in $|A_0^{\pm}|$ occurring for single-row periodic arrays (figure 12). In single-row periodic arrays, the narrow-banded feature is only present for arrays with freely oscillating bodies; it is smoothed out when the bodies are extracting energy, and it is absent for fixed bodies. Furthermore, the free-surface elevation amplitude $|\eta|$ is much lower in the perfect reflection case (figure 15*a*), compared to $|\eta|$ at trapped-wave wavenumbers (figure 23*a*,*c*,*d*).

The amplitude of the free-surface elevation $|\eta|$ for the three configurations at specific wavenumbers for $\theta_I = 0°$ is shown in figure 23. The free-surface amplitude around the configuration-II array at its first trapped-wave wavenumber (figure 23*a*) shows very high elevation ($|\eta| \sim 10.7$) around bodies 1 and 3. Body 1 extracts most of the energy (and undergoes largest heave motions $|X_1|$), while body 2 extracts almost no energy at all (i.e. is barely moving). The high q achieved in this case is manifested by a significant decrease in $|\eta|$ everywhere behind the array. For configuration II, we also consider two distinct wavenumbers around the second trapped-wave wavenumber, one from each side of the (asymmetric) jump: $kd = 2.08\pi$ before the jump, corresponding to the higher q value (figure 23*b*), and $kd = 2.10\pi$ after the jump, corresponding to the lower q value (figure 23*c*). In this case, high-q values do not correspond to high-$|\eta|$ values – $|\eta|$ is higher for the low-q case. The high elevation $|\eta|$ occurs around bodies 1 and 3, but also between the bodies in the second row. Furthermore, the distribution of power among the bodies is different between the two wavenumbers: in the high-q case the middle body extracts the most

https://doi.org/10.1017/jfm.2018.911 Published online by Cambridge University Press

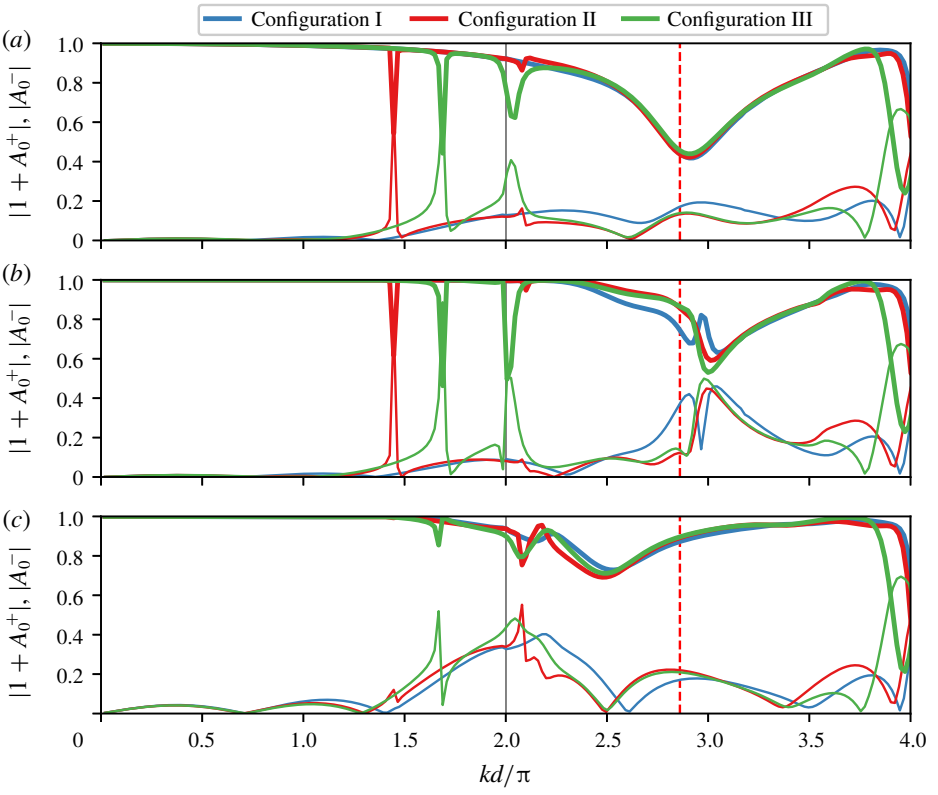

FIGURE 22. The transmitted $|A_0^+|$ (thick lines) and reflected mode $|A_0^-|$ (thin lines) amplitudes for three-row periodic arrays of truncated vertical cylinders at $\theta_I = 0°$ incidence. (*a*) Energy-extracting bodies; (*b*) freely oscillating bodies; (*c*) fixed bodies. Rayleigh wavenumber (indistinguishable difference in $(kd)_1^{cr}$ between the three configurations) is marked by a grey vertical line; body-resonant wavenumber by a dashed red line.

power, while in the low-q case, the middle body is barely moving. Overall, the performance of the array is starkly different across the Fano feature.

The free-surface amplitude at the first and second trapped-wave wavenumbers for configuration III (figure 23*d*,*e*) follows a similar pattern to that of configuration II. For both trapped-wave wavenumbers, the middle body extracts almost no energy (i.e. is barely moving), with the highest elevations occurring at bodies 1 and 3. At the body-resonant wavenumber $k_r a$, all the bodies in configuration I extract energy equally (figure 23*f*). The free-surface elevation behind the array is significantly reduced, which, together with a relatively mild modulation of the free surface in front, indicates efficient energy extraction and a high q value.

The amplitude of free-surface elevation along the x and y axes for configurations I and II is shown in figure 24. For configuration I, the free surface is shown for the body-resonant wavenumber $k_r a$ where there is significant energy extraction. The free-surface amplitude behind the array exhibits much longer modulation compared to that in front. The mean amplitude along a row, i.e. along $x = 0, d_x, 2d_x$, is generally decreasing for larger x. For configuration II, $|\eta|$ is shown for $kd = 1.45\pi$, which corresponds to the first trapped-wave wavenumber (cf. figure 23*a*), and for $kd = 2.08\pi$ and 2.10π, corresponding to wavenumbers surrounding the second trapped-wave

https://doi.org/10.1017/jfm.2018.911 Published online by Cambridge University Press

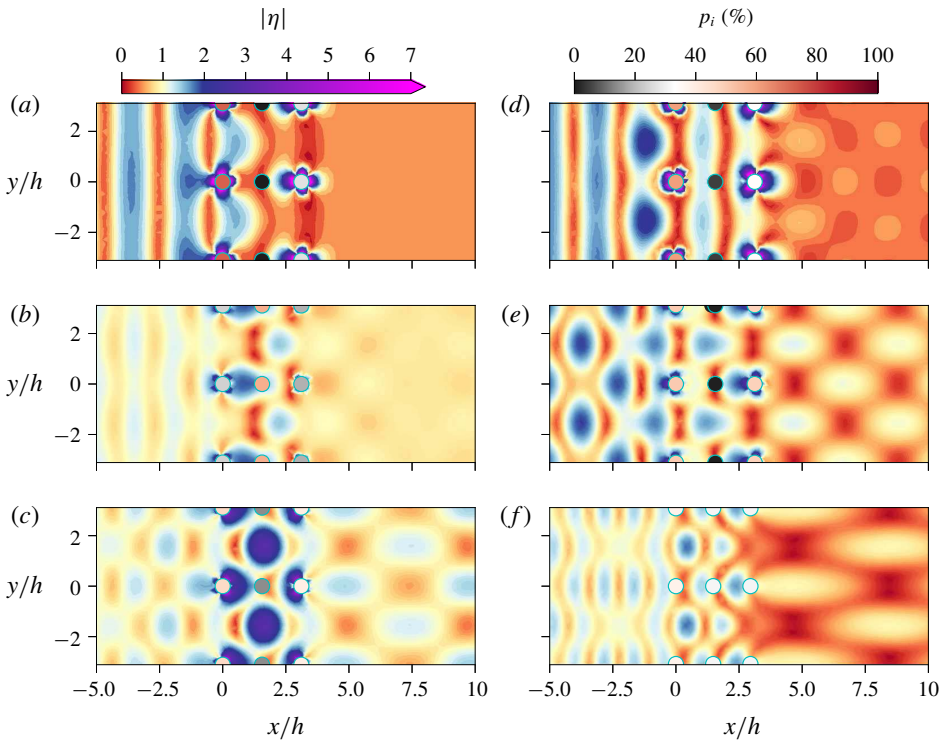

FIGURE 23. Free-surface amplitude $|\eta|$ contours for three slightly perturbed configurations of three-row truncated-vertical-cylinder periodic arrays at specific wavenumbers, for $\theta_I = 0°$. (*a*) Configuration II, $kd = 1.45\pi$. (*b*) Configuration II, $kd = 2.08\pi$. (*c*) Configuration II, $kd = 2.10\pi$. (*d*) Configuration III, $kd = 1.69\pi$. (*e*) Configuration III, $kd = 2.05\pi$. (*f*) Configuration I, $kd = 2.86\pi$. The body colour denotes the power extraction percentage p_i of each body (according to the right colour bar).

wavenumber (cf. figure 23*b*,*c*). High free-surface elevations at the cylinder surface are visible for the first trapped-wave wavenumber, as well as the high elevation in between the bodies in the second row at the third wavenumber ($kd = 2.10\pi$).

We remark on the numerical convergence of the results in this section. As in § 5, the results presented in this section generally converge to $O(1\,\%)$. The exceptions are the values obtained for wavenumbers close to kd^{RB}, where the qualitative conclusions about the Rayleigh–Bloch waves remain valid as the number of modes in partial wave decomposition is increased, although the quantitative values may be affected. We also note that the large free-surface elevations due to Rayleigh–Bloch waves indicate that the linear wave theory is not strictly valid at those wavenumbers because the small-wave-steepness assumption is violated. For an accurate analysis of array performance at trapped-wave wavenumbers, one should conduct nonlinear computations based on the models that include nonlinear wave dynamics and wave–body interactions.

Finally, we remark that while we focus here on the three-row periodic WEC arrays only, we have performed similar computations (and analyses) for two- and four-row periodic arrays (not presented). The results for these configurations show a similar character as those for the three-row arrays presented here, including the decrease in the array gain at Rayleigh, Bragg and Laue resonances, as well as the

https://doi.org/10.1017/jfm.2018.911 Published online by Cambridge University Press

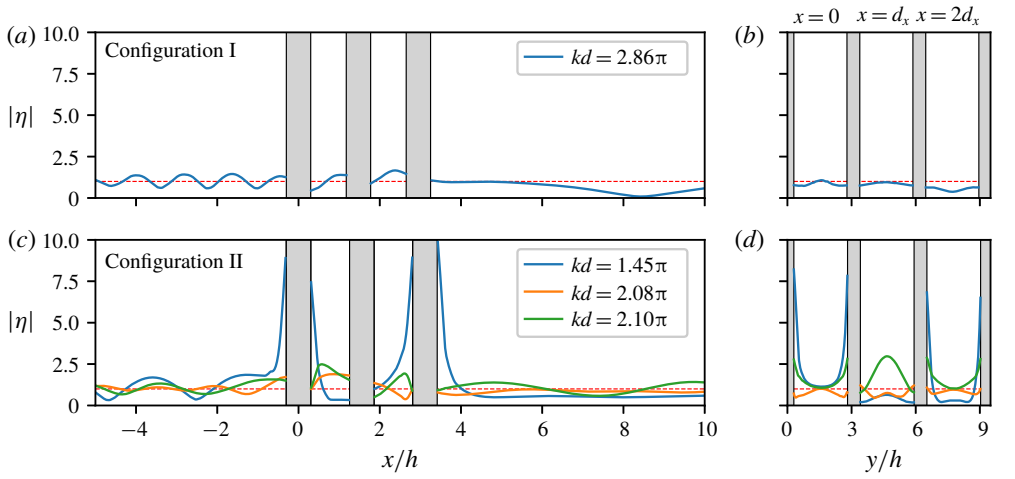

FIGURE 24. Free-surface amplitude $|\eta|$ for two slightly perturbed configurations of three-row truncated-vertical-cylinder periodic arrays at specific wavenumbers, for $\theta_I = 0°$. The amplitude is plotted for $y = 0$ (*a*,*c*) and at three different $x = \text{const.}$ (*b*,*d*). Grey vertical bars in both views denote the locations of the bodies.

presence of embedded motion-trapped Rayleigh–Bloch waves for configurations with $d_x/d \approx 1/(N-1)$. Furthermore, our choice of the body shape is purely arbitrary and not special in any way. This indicates that these findings should also be valid for arrays consisting of bodies of general (axisymmetric) shape.

7. Conclusion

We conduct a systematic parametric study of array configurations of single- and multi-row periodic WEC arrays in the context of linear potential flow. We consider important physical phenomena that strongly affect the energy extraction performance of point-absorber periodic arrays and periodic arrays of general WEC geometries and power take-off rates. Some of these phenomena (Rayleigh and Bragg resonances) have been discussed before in the WEC array context, but we extend here the understanding and validity of those discussions. Some phenomena – Laue resonances and embedded motion-trapped Rayleigh–Bloch waves – have not been discussed before in the WEC-array context. An important development is a new multiple-scattering method for periodic arrays consisting of sub-arrays of bodies of general shape. The method fully accounts for wave–body interactions, including evanescent waves and close-spacing effects. The method also allows the analysis of performance of each of the bodies in the array (motion and force amplitudes, individually extracted powers) as well as the calculation of the near- and far-field free surface.

Using both theoretical considerations and extensive computations based on the new exact interaction method, we analyse the effect of spatial configuration on the array performance in monochromatic waves. For a single periodic row, we show that the array gain q of a realistic WEC array of truncated vertical cylinders closely matches that of optimal point-absorber arrays, although not reaching the same maximum values. At Rayleigh wavenumbers, $q = 0$ for both array types. We also identify an interesting result where a single row of freely oscillating bodies can act as a perfect reflector of the incident wave for a range of incident angles.

https://doi.org/10.1017/jfm.2018.911 Published online by Cambridge University Press

For multi-row periodic arrays, we relate the significant reductions in the achieved array gain q, away from Rayleigh wavenumbers, to Laue and Bragg resonances. Laue resonances have not been identified in the WEC array context before, and we show that they cause a large, smooth decrease in q for wavenumbers around the resonance condition. Where different Laue resonances coincide, the decrease in q is larger and of wider bandwidth. We also show that the reductions in gain due to Bragg resonances can be appreciable even for a small number of strong absorbers, in contrast to the previously discussed case for a large number of rows of weakly absorbing bodies. We show that these phenomena are persistent in rectangular periodic arrays, regardless of whether they are point-absorber ones or those consisting of general, finite bodies in non-optimal motion.

The most significant difference between the multi-row point-absorber arrays and multi-row arrays of truncated vertical cylinders is the presence of embedded motion-trapped Rayleigh–Bloch waves, which occur only in the latter case. Our development of a computational method that is capable of exactly accounting for wave–body interactions in periodic arrays is crucial for finding these heretofore undiscovered trapped waves. We provide evidence of their existence in rectangular arrays with an aspect ratio $(N-1)d_x/d \approx 1$, being excited by an incident planar wave (not necessarily normal). For a given array configuration that can support Rayleigh–Bloch waves, these Rayleigh–Bloch waves occur for isolated wavenumbers and incident angles. A perturbation in spatial configuration that preserves the aspect ratio of the array does not destroy them but merely makes them occur at a different wavenumber and incident angle. In WEC arrays, Rayleigh–Bloch waves lead to a sharp increase in the array gain q at wavenumbers where they occur. These waves are also present in arrays of freely oscillating or fixed bodies, in which cases they lead to abrupt changes in reflection and transmission coefficients.

We remark that while the analysis conducted here is for relatively simple bodies (truncated cylinders) and motions (heave only), the multiple-scattering method applies to general body geometries and motions. We postulate that the general conclusions on Bragg and Laue resonances would hold even for more complicated body geometries and for arrays consisting of different body types, provided that the bodies are arranged in a lattice-like configuration (as it holds, for example, in polyatomic crystals (Ashcroft & Mermin 1976)). Finally, while we have focused here on monochromatic incident waves only, the analyses and computations generalize in a straightforward way to studying array performance in irregular (directional) seas and are presented in Tokić (2016).

The present results are useful for practical design of WEC arrays. For example, they provide an insight into how to design an array configuration to achieve high gain q, while avoiding the resonances that lead to significant decreases in q. In practice, additional factors may be of importance. For example, the trade-off between q (relevant for effectiveness of the installed devices) and the capture width W_a/d (relevant for the total extracted energy per unit of coastline) may need to be carefully considered. The computational method presented in this work can be directly applied to such analyses.

Acknowledgement

This research is supported financially by a grant from the US Office of Naval Research N000141512460.

https://doi.org/10.1017/jfm.2018.911 Published online by Cambridge University Press

Appendix A. Derivation of the multiple-scattering formulation

For simplicity of exposition, we first present the diffraction problem for periodic arrays (i.e. for arrays of fixed bodies); the extension to oscillating (and energy extracting) bodies is made in § A.1. In general, the total potential Φ for a periodic array of fixed bodies can be written as

$$\Phi = \Phi^I + \phi^S = \Phi^I + \sum_{\hat{\jmath}\in\mathbb{Z}} \Phi^{S,\hat{\jmath}}, \tag{A 1}$$

where Φ^I represents the incoming planar wave potential, $\Phi^{S,\hat{\jmath}}$ the scattering potential of body $\mathcal{B}_{\hat{\jmath}}$, and ϕ^S the total scattering potential. We label the bodies by the index $\hat{\jmath}$ in a cell-first manner, i.e. such that we first label all the bodies within cell B before moving to cell $B+1$; $B=0$ denotes the cell where the origin of the coordinate system is, say (figure 6). The labelling within a cell is done in the same manner for every B. With this convention, we can relate a general body index $\hat{\jmath}$ to an index j in the basic cell $B=0$ by

$$\left.\begin{aligned} B &= \left\lfloor \frac{\hat{\jmath}}{N} \right\rfloor \\ j &= \hat{\jmath} - BN, \end{aligned}\right\} \tag{A 2}$$

where $\lfloor\cdot\rfloor$ denotes the floor function.

The total potential in the reference frame of body $\mathcal{B}_p$ can also be written as $\Phi = \Phi^{I,p} + \Phi^{S,p}$, where

$$\Phi^{I,p}(\boldsymbol{r}_p) = \Phi^I + \sum_{\hat{\jmath}\in\mathbb{Z},\,\hat{\jmath}\neq p} \Phi^{S,\hat{\jmath}}(\boldsymbol{r}_{\hat{\jmath}}) \tag{A 3}$$

is the incoming potential at $\mathcal{B}_p$, consisting of the ambient incoming wave and of the scattered waves from all the other bodies in the array. The body $\mathcal{B}_p$ can be in the basic cell $B=0$, without the loss of generality. We can expand the potentials near $\mathcal{B}_p$ in terms of radial incident and outgoing partial waves, i.e. Hankel functions and modified Bessel functions, which are fundamental solutions of the Helmholtz equation. In the cylindrical coordinate system (r_p, ϑ_p, z) of body $\mathcal{B}_p$, the general incident and scattering potentials can be written as

$$\Phi^{I,p} = \sum_{m,n} \boldsymbol{d}^p_{mn} \mathrm{I}_n(k_m r_p) \mathrm{e}^{\mathrm{i}n\vartheta_p} \psi_m(z), \tag{A 4a}$$

$$\Phi^{S,p} = \sum_{m,n} \boldsymbol{c}^p_{mn} \mathrm{K}_n(k_m r_p) \mathrm{e}^{\mathrm{i}n\vartheta_p} \psi_m(z), \tag{A 4b}$$

where $\mathrm{I}_n(z)$ and $\mathrm{K}_n(z)$ are the modified Bessel function of the first and the second kind, $\boldsymbol{d}^j_{nm}$ and $\boldsymbol{c}^j_{nm}$ are the coefficients of the incident and outgoing (scattered) partial waves, $\psi_m(z)$ is the finite-depth eigenfunction (Mei *et al.* 2005), and

$$\sum_{m,n} \equiv \sum_{m=0}^{\infty} \sum_{n=-\infty}^{\infty}. \tag{A 5}$$

In the above expressions, $m=0$ corresponds to the propagating mode with a wavenumber $k_0 \equiv -\mathrm{i}k$, while $m>0$ corresponds to the evanescent modes with wavenumbers k_m that are the real solutions of the modified dispersion relation

https://doi.org/10.1017/jfm.2018.911 Published online by Cambridge University Press

$\omega^2 = -gk_m \tan k_m h$. We have also used the well-known identities between modified Bessel functions and Hankel and Bessel functions

$$\left.\begin{aligned} \mathrm{K}_n(-\mathrm{i}k) &= \frac{\pi}{2}\mathrm{i}^{n+1}\mathrm{H}_n^{(1)}(k) \\ \mathrm{I}_n(-\mathrm{i}k) &= \mathrm{i}^{-n}\mathrm{J}_n(k) \end{aligned}\right\} \tag{A 6}$$

to simplify the expressions. Hankel function $\mathrm{H}_n^{(1)}(x) = \mathrm{J}_n(x) + \mathrm{i}\mathrm{Y}_n(x)$ represents an outward propagating wave. We expand ϕ^I into partial waves around $\mathcal{B}_p$ in a similar way to obtain

$$\phi^I(\boldsymbol{r}_p) = \sum_{n=-\infty}^{\infty} d_n^{I,p}\mathrm{I}_n(k_0 r_p)\mathrm{e}^{\mathrm{i}n\vartheta_p}\psi_0(z), \quad d_n^{I,p} \equiv P_p(-1)^n\mathrm{e}^{-\mathrm{i}n\theta_I}, \tag{A 7}$$

where $d_n^{I,p}$ are the (known) coefficients of the incident wave decomposition, and $P_p = \mathrm{e}^{\mathrm{i}kR_p\cos(\theta_I-\alpha_p)}$ is the phase of the incident wave at $\mathcal{B}_p$. Combining (A 3) and (A 7), $\Phi^{I,p}$ becomes

$$\Phi^{I,p} = \sum_{n=-\infty}^{\infty} d_n^{I,p}\mathrm{I}_n(k_0 r_p)\mathrm{e}^{\mathrm{i}n\vartheta_p}\psi_0(z) + \sum_{\substack{\hat{\jmath}\in\mathbb{Z},\\ \hat{\jmath}\neq p}}\sum_{m,n} c_{mn}^{\hat{\jmath}}\mathrm{K}_n(k_m r_{\hat{\jmath}})\mathrm{e}^{\mathrm{i}n\vartheta_{\hat{\jmath}}}\psi_m(z). \tag{A 8}$$

We can transform the body $\mathcal{B}_{\hat{\jmath}}$-based coordinate system $(r_{\hat{\jmath}}, \vartheta_{\hat{\jmath}}, z)$ into a $\mathcal{B}_p$-based (r_p, ϑ_p, z) coordinate system by using Graf addition theorem for Bessel functions (Abramowitz & Stegun 1964)

$$\mathrm{K}_n(k_m r_{\hat{\jmath}})\mathrm{e}^{\mathrm{i}n\vartheta_{\hat{\jmath}}} = \sum_{l=-\infty}^{\infty}(-1)^l\mathrm{K}_{n-l}(k_m R_{\hat{\jmath}p})\mathrm{e}^{\mathrm{i}(n-l)\alpha_{\hat{\jmath}p}}\mathrm{I}_l(k_m r_p)\mathrm{e}^{\mathrm{i}l\vartheta_p}, \quad r_p < R_{\hat{\jmath}p}, \tag{A 9}$$

where $R_{\hat{\jmath}p}$ is the distance between bodies $\hat{\jmath}$ and p, and $\alpha_{\hat{\jmath}p}$ the angle between them, figure 6. Comparing the potential $\Phi^{I,p}$ with (A 4*a*) results in an expression for the incident partial wave coefficients for $\mathcal{B}_p$

$$\boldsymbol{d}_{ml}^p = \delta_{m0}d_l^{I,p} + \sum_{\substack{\hat{\jmath}\in\mathbb{Z},\\ \hat{\jmath}\neq p}}\sum_{n=-\infty}^{\infty}(-1)^l c_{mn}^{\hat{\jmath}}\mathrm{K}_{n-l}(k_m R_{\hat{\jmath}p})\mathrm{e}^{\mathrm{i}(n-l)\alpha_{\hat{\jmath}p}}, \tag{A 10}$$

where δ_{mn} is the Kronecker delta.

The summation over infinite number of bodies in (A 10) can be simplified by reorganizing the summation itself and by using Bloch's theorem (2.1). First, the summation can be split into two by recognizing

$$\sum_{\substack{\hat{\jmath}\in\mathbb{Z},\\ \hat{\jmath}\neq p}} = \sum_{\substack{j=1,\\ j\neq p,\\ B=0}}^{N} + \sum_{\substack{B=-\infty,\\ B\neq 0}}^{\infty}\sum_{j=1}^{N}. \tag{A 11}$$

Second, we can use (2.1) to relate the scattering coefficients of body $\hat{\jmath}$ to those of body j through

$$c_{mn}^{\hat{\jmath}} = c_{mn}^{j}P_B, \tag{A 12}$$

https://doi.org/10.1017/jfm.2018.911 Published online by Cambridge University Press

where $P_B \equiv \mathrm{e}^{\mathrm{i}Bkd\sin\theta_I}$ is the phase factor for cell B. The decomposition (A 11) splits the summation over all bodies into the summation over a finite number of bodies in the basic ($B=0$) cell and the summation over all the other bodies.

With (A 11) and (A 12), the second term in (A 10) becomes

$$\sum_{\substack{j=1,\\ j\neq p,\\ B=0}}^{N}\sum_{n=-\infty}^{\infty} \boldsymbol{c}^{j}_{mn}(\boldsymbol{S}^{jp})_{n,l,m} + (-1)^{l}\sum_{j=1}^{N}\sum_{n=-\infty}^{\infty}\boldsymbol{c}^{j}_{mn}\sum_{\substack{B=-\infty,\\ B\neq 0}}^{\infty} P_B \mathrm{K}_{n-l}(k_m R_{\hat{j}p})\mathrm{e}^{\mathrm{i}(n-l)\alpha_{\hat{j}p}}, \tag{A 13}$$

where $(\boldsymbol{S}^{jp})_{n,l,m}$ represents elements of a separation matrix $\boldsymbol{S}^{jp}$ for bodies $\mathcal{B}_j$ and $\mathcal{B}_p$

$$(\boldsymbol{S}^{jp})_{n,l,m} = (-1)^{l}\mathrm{K}_{n-l}(k_m R_{jp})\mathrm{e}^{\mathrm{i}(n-l)\alpha_{jp}}. \tag{A 14}$$

The separation matrix only depends on the relative position between the two bodies in a sub-array and is, thus, identical to that for scattering by a finite array (Kagemoto & Yue 1986).

The second term in (A 13) needs further treatment because the summation indices j and B are not explicitly expressed in $R_{\hat{j}p}$ and $\alpha_{\hat{j}p}$. That can be rectified by considering the decomposition of the distance vector $\boldsymbol{R}_{\hat{j}p}$ into

$$\boldsymbol{R}_{\hat{j}p} = \boldsymbol{R}_{\hat{j}j} + \boldsymbol{R}_{jp}, \tag{A 15}$$

where $\boldsymbol{R}_{\hat{j}j} = -Bd\,\boldsymbol{e}_y$, figure 6(*a*). For the case when $|\boldsymbol{R}_{\hat{j}j}| > |\boldsymbol{R}_{jp}|$, which is certainly valid for large B, Graf's addition theorem (A 9) applied to vectors in (A 15) gives

$$\mathrm{K}_{\mu}(k_m R_{\hat{j}p})\mathrm{e}^{\mathrm{i}\mu\alpha_{\hat{j}p}} = \sum_{\nu=-\infty}^{\infty}(-1)^{\nu}\mathrm{K}_{\mu-\nu}(k_m|B|d)\mathrm{e}^{\mathrm{i}(\mu-\nu)\alpha_B}\mathrm{I}_{\nu}(k_m R_{jp})\mathrm{e}^{\mathrm{i}\nu\alpha_{jp}}, \tag{A 16}$$

where

$$\alpha_B = \begin{cases} -\dfrac{\pi}{2}, & B>0 \\ \dfrac{\pi}{2}, & B<0. \end{cases} \tag{A 17}$$

Let us first consider the case where the maximal distance between the bodies in a cell is smaller than the periodicity d, i.e. $\max\{R_{jp} : j, p \in \{1,\ldots,N\}\} < d$. In that case, the expression (A 16) is valid for all cells B, and the second sum in (A 13) becomes $\sum_{j=1}^{N}\sum_{n=-\infty}^{\infty} c^{j}_{nm}(\boldsymbol{Q}^{jp})_{n,l,m}$, where $(\boldsymbol{Q}^{jp})_{n,l,m}$ represents the elements of a periodicity matrix $\boldsymbol{Q}^{jp}$ for bodies j and p

$$(\boldsymbol{Q}^{jp})_{n,l,m} \equiv (-1)^{l}\sum_{\nu=-\infty}^{\infty}(-\mathrm{i})^{\mu+\nu}\mathrm{I}_{\nu}(k_m R_{jp})\mathrm{e}^{\mathrm{i}\nu\alpha_{jp}}\sigma_{\mu-\nu,m}(\theta_I, d), \quad \mu \equiv n-l, \tag{A 18}$$

and $\sigma_{n,m}$ is the so-called lattice sum (or Schlömilch sum) (Linton 1998)

$$\sigma_{n,m}(\theta_I, d) = \sum_{B=1}^{\infty}[P_B + (-1)^{n}P_{-B}]\mathrm{K}_n(Bk_m d). \tag{A 19}$$

The lattice sum $\sigma_{n,m}$ depends only on the periodicity d of the lattice and the incident wave angle θ_I, and not on the number of bodies in the sub-array $\mathcal{A}$ or on its

https://doi.org/10.1017/jfm.2018.911 Published online by Cambridge University Press

spatial configuration. For evanescent waves ($m > 0$), it can be summed directly as it converges rapidly. For propagating waves ($m = 0$), we use an accelerated expression to evaluate (A 19) (Linton 1998), otherwise the sum is extremely slowly convergent; for evanescent waves ($m > 0$), (A 19) can be summed directly.

If $R_{jp} > d$, (A 18) has to be modified. Let B_R denote the largest integer B for which the condition $R_{jp} > |B|d$ is valid. The Graf addition theorem (A 16) can then be applied only for $|B| > B_R$ terms in the second summand of (A 13), while the sum over the finite number of terms $|B| = 1, \ldots, B_R$ is left in its original form. This results in the modified expression for $(\boldsymbol{Q}^{jp})_{n,l,m}$

$$(\boldsymbol{Q}^{jp})_{n,l,m} \equiv (-1)^l \sum_{\nu=-\infty}^{\infty} (-\mathrm{i})^{\mu+\nu} \mathrm{I}_\nu(k_m R_{jp}) \mathrm{e}^{\mathrm{i}\nu\alpha_{jp}} \sigma'_{\mu-\nu,m}(\theta_I, d), \\ + (-1)^l \sum_{\substack{B=-B_R, \\ B\neq 0}}^{B_R} P_B \mathrm{K}_\mu(k_m R_{\hat{j}p}) \mathrm{e}^{\mathrm{i}\mu\alpha_{\hat{j}p}}, \quad \mu \equiv n - l, \tag{A 20}$$

where $\sigma'_{n,m}(\theta_I, d)$ is the corrected lattice sum

$$\sigma'_{n,m}(\theta_I, d) = \sigma_{n,m}(\theta_I, d) - \sum_{B=1}^{B_R} [P_B + (-1)^n P_{-B}] \mathrm{K}_n(Bk_m d). \tag{A 21}$$

The finite sum in (A 21) accounts for the terms that had to be added to the infinite sum over the bodies (that initially excludes $|B| = 1, \ldots, B_R$ cells) to cast it into a true Schlömilch sum $\sigma_{n,m}$ for which fast analytical expressions exist. While the formulation (A 20) is in theory convergent as the infinite sum over ν contains only the contributions from bodies for which Graf's addition formula (A 16) is valid, a floating-problem arithmetic problem occurs when calculating $\sigma'_{n,m}(\theta_I, k_m d)$ for large n that arise in the summation over ν. As a result, the infinite sum in (A 20) is polluted and its convergence deteriorates.

Adding all together, the coefficients of the incident partial waves on $\mathcal{B}_p$ can be written as

$$d^p_{ml} = \delta_{m0} d^{I,p}_l + \sum_{\substack{j=1, \\ j\neq p, B=0}}^{N} \sum_{n=-\infty}^{\infty} c^j_{mn} (\boldsymbol{S}^{jp})_{n,l,m} + \sum_{j=1}^{N} \sum_{n=-\infty}^{\infty} c^j_{mn} (\boldsymbol{Q}^{jp})_{n,l,m}, \\ = \delta_{m0} d^{I,p}_l + \sum_{j=1}^{N} \sum_{n=-\infty}^{\infty} ((1 - \delta_{jp})(\boldsymbol{S}^{jp})_{n,l,m} + (\boldsymbol{Q}^{jp})_{n,l,m}) c^j_{mn}. \tag{A 22}$$

The scattered and incident wave coefficients c^p_{nm}, d^p_{nm} are related by (4.1), through the $\boldsymbol{T}$-matrix of body $\mathcal{B}_p$. Thus, we obtain a linear system for the unknown coefficients of the scattered partial waves on body $\mathcal{B}_p$ as

$$\sum_{j=1}^{N} [\delta_{jp} - \boldsymbol{T}^p ((1 - \delta_{jp}) \boldsymbol{S}^{jp} + \boldsymbol{Q}^{jp})^{\mathrm{T}}] \boldsymbol{c}^j = \boldsymbol{T}^p \boldsymbol{d}^{\boldsymbol{I},p}, \quad p = 1, \ldots, N. \tag{A 23}$$

The global system is obtained when (A 23) is constructed for all bodies in the sub-array, resulting in a global form

$$(\boldsymbol{I} - \boldsymbol{T}(\boldsymbol{S} + \boldsymbol{Q})^{\mathrm{T}}) \boldsymbol{c} = \boldsymbol{T} \boldsymbol{d}, \tag{A 24}$$

which is the fixed-body version of (4.2).

https://doi.org/10.1017/jfm.2018.911 Published online by Cambridge University Press

A.1. *Modification for oscillating bodies*

If the bodies in a periodic array are allowed to oscillate, the total potential Φ can be written as

$$\Phi = \Phi^I + \phi^S = \Phi^I + \sum_{\hat{\jmath}\in\mathbb{Z}} \left(\Phi^{S,\,\hat{\jmath}} + \sum_k \boldsymbol{V}_k^{\hat{\jmath}} \Phi_k^{R,\,\hat{\jmath}} \right), \tag{A 25}$$

where the new component is the radiation potential $\Phi_k^{R,\,\hat{\jmath}}$ of body $\hat{\jmath}$ oscillating in mode k with a unit velocity amplitude, and $\boldsymbol{V}_k^{\hat{\jmath}}$ is the actual complex velocity in mode k of body $\hat{\jmath}$. Mode k denotes one of six degrees of freedom ($k \in \mathcal{K}_{\hat{\jmath}}$; $\mathcal{K}_{\hat{\jmath}} \subseteq \mathcal{D} = \{1, 2, \ldots, 6\}$), where directions 1, 2, 3 correspond to the translation modes of motion (surge, sway, heave) and 4, 5, 6 to the rotational modes (roll, pitch, yaw).

Analogous to (A 4), we can express the radiation potential of body $\mathcal{B}_p$ as

$$\Phi_k^{R,\,p} = \sum_{m,n} c_{mn}^{R,k,p} \mathrm{K}_n(k_m r_p) \mathrm{e}^{\mathrm{i}n\vartheta_p} \psi_m(z), \tag{A 26}$$

where $c_{nm}^{R,k,p}$ are the coefficients of the radiated, outgoing partial waves due to unit velocity of body $\mathcal{B}_p$ in direction k. These are the elements on the radiated wave coefficient matrix $\boldsymbol{c}^{\boldsymbol{R}p}$, which depends solely on the isolated-body properties so it can be calculated beforehand.

The linear equation of motion of a body in the frequency domain is given by (cf. (4.5))

$$[-\omega^2(\boldsymbol{M}_b + \boldsymbol{M}_a(\omega)) - \mathrm{i}\omega(\boldsymbol{\Lambda}(\omega) + \boldsymbol{B}_{PTO}) + (\boldsymbol{C} + \boldsymbol{C}_{PTO})] \cdot \boldsymbol{X} = \boldsymbol{A} \cdot \boldsymbol{X} = \boldsymbol{F}(\omega), \tag{A 27}$$

where $\boldsymbol{A}$ is the body dynamics matrix, $\boldsymbol{M}_b$ is the mass matrix, $\boldsymbol{M}_a(\omega)$ and $\boldsymbol{\Lambda}(\omega)$ are the conventional real-valued, frequency-dependent added mass and radiation damping matrices of the body obtained from a complex restoring force matrix (Mei *et al.* 2005), $\boldsymbol{B}_{PTO}$ and $\boldsymbol{C}_{PTO}$ are the PTO extraction rate and stiffness matrices, $\boldsymbol{C}$ is the restoring coefficient matrix due to the changes in buoyancy, $\boldsymbol{X}$ is the complex motion amplitude and $\boldsymbol{F}(\omega)$ is the diffraction force. While the optimal power extraction can be determined from excitation force alone (e.g. Evans 1976), for non-optimal power extraction the full equation of motion (A 27) is needed. We note that obtaining the optimal b_{PTO} distribution for a WEC array based on (A 27), while possible in principle, is a non-trivial task due to the dependency of $\boldsymbol{F}(\omega)$ on motion (and, thus, on b_{PTO} values) of other bodies.

Since the radiation potential (A 26) is of the same form as the scattered potential (A 4*b*), it can easily be incorporated into the derivation for fixed bodies presented above. We only have to replace the vector of scattered wave coefficients $\boldsymbol{c}^j$ in (A 22) with

$$\boldsymbol{c}^j \to (\boldsymbol{I} + \boldsymbol{c}^{\boldsymbol{R}j} \cdot \boldsymbol{\varpi}^{j\mathrm{T}})\boldsymbol{c}^j = \boldsymbol{H}^j \cdot \boldsymbol{c}^j, \tag{A 28}$$

where we used (4.4)–(4.7) to relate $\boldsymbol{V}^j$ to $\boldsymbol{c}^j$. This effectively casts (A 25) into (A 1). The derivation otherwise proceeds analogously. In the end, by combining (A 22) and (A 28), we obtain the global system equation (4.2).

In the computations presented in this study, we only focused on a single degree-of-freedom motion so (A 27) reduces to a scalar equation, and matrices $\boldsymbol{A}$, $\boldsymbol{M}_b$, $\boldsymbol{M}_a$, $\boldsymbol{\Lambda}$, $\boldsymbol{B}_{PTO}$, $\boldsymbol{C}_{PTO}$ and $\boldsymbol{C}$ reduce to scalars. In our calculations, $\boldsymbol{C}_{PTO} = 0$ and $\boldsymbol{B}_{PTO} = b_{PTO}$. For a truncated cylinder of radius a, $\boldsymbol{C} = \rho g a^2 \pi$.

https://doi.org/10.1017/jfm.2018.911 Published online by Cambridge University Press

A.2. *Transmission and reflection coefficients*

The total scattering potential of the entire periodic array is

$$\phi^S = \sum_{\hat{\jmath}\in\mathbb{Z}} \sum_{n=-\infty}^{\infty} \sum_{m=0}^{\infty} c^{\hat{\jmath}}_{mn} \mathrm{K}_n(k_m r_{\hat{\jmath}}) \mathrm{e}^{\mathrm{i}n\vartheta_{\hat{\jmath}}} \psi_m(z). \tag{A 29}$$

Far away from the array, i.e. $|x| \to \infty$, evanescent waves are absent, and, using (A 2), (A 12) and Bessel function identities (A 6), the (A 29) simplifies to

$$\phi^S = \frac{\mathrm{i}\pi}{2} \psi_0(z) \sum_{n=-\infty}^{\infty} \sum_{j=1}^{N} c^j_{0n} \sum_{B=-\infty}^{\infty} P_B \mathrm{H}_n(kr_{j,B}) \mathrm{i}^n \mathrm{e}^{\mathrm{i}n\vartheta_{j,B}}, \tag{A 30}$$

where we have retained only the propagating $m = 0$ mode and expressed it in terms of Hankel function ($k = |k_0|$); $(r_{j,B}, \vartheta_{j,B})$ refers to the cylindrical coordinate system of body j in cell B (according to (A 2)). We can further simplify this expression using the Sommerfeld integral representation of Hankel function (Sommerfeld 1964)

$$\mathrm{H}_n(kr_{j,B}) \mathrm{e}^{\mathrm{i}n\vartheta_{j,B}} \mathrm{i}^n = \frac{1}{\pi} \int_{-\infty}^{\infty} \mathrm{e}^{\mathrm{i}k(y_j - Bd)t} \mathrm{e}^{\mathrm{i}kx_j\sqrt{1-t^2}} \frac{\mathrm{e}^{\mathrm{i}n \arcsin t}}{\sqrt{1-t^2}} \,\mathrm{d}t \tag{A 31}$$

and the Poisson summation formula

$$\sum_{B=-\infty}^{\infty} \int_{-\infty}^{\infty} f(t) \mathrm{e}^{-\mathrm{i}2\pi Bt} \,\mathrm{d}t = \sum_{\mu=-\infty}^{\infty} f(\mu). \tag{A 32}$$

To cast $P_B \mathrm{H}_n(kr_{j,B}) \mathrm{i}^n \mathrm{e}^{\mathrm{i}n\vartheta_{j,B}}$ in the form required for (A 32), we set $f(t;\, x_j,\, y_j) = \mathrm{e}^{\mathrm{i}ky_j t} \mathrm{e}^{\mathrm{i}kx_j\sqrt{1-t^2}} \mathrm{e}^{\mathrm{i}n \arcsin t} / \sqrt{1-t^2}$ and use substitution $t = \gamma(t') = \sin\theta_I + 2\pi t'/kd$. This results in

$$\sum_{B=-\infty}^{\infty} P_B \mathrm{H}_n(kr_{j,B}) \mathrm{e}^{\mathrm{i}n\vartheta_{j,B}} \mathrm{i}^n = \frac{2}{kd} \sum_{\mu=-\infty}^{\infty} f(\gamma(\mu);\, x_j,\, y_j). \tag{A 33}$$

However, for $f(\gamma(\mu); x_j, y_j)$ to be finite as $x_j \to \infty$, $|\gamma(\mu)| \leqslant 1$. This is only possible for $\mu \in \mathcal{M}(\theta_I, kd)$, where $\mathcal{M}$ is the set of all the indices of propagating modes in the far field introduced in (2.4). Recognizing that $\gamma(\mu) = \sin\theta_\mu$, we obtain

$$\sum_{B=-\infty}^{\infty} P_B \mathrm{H}_n(kr_{j,B}) \mathrm{e}^{\mathrm{i}n\vartheta_{j,B}} \mathrm{i}^n = \frac{2}{kd} \sum_{\mu\in\mathcal{M}} \frac{\mathrm{e}^{\mathrm{i}(kx_j \cos\theta_\mu + ky_j \sin\theta_\mu)}}{\cos\theta_\mu} \mathrm{e}^{\mathrm{i}n\theta_\mu}. \tag{A 34}$$

We transform the coordinates from the body $\mathcal{B}_j$-coordinate system into the global one to obtain $kx_j \cos\theta_\mu + ky_j \sin\theta_\mu = kr\cos(\vartheta - \theta_\mu) - kR_j \cos(\alpha_j - \theta_\mu)$, where (R_j, α_j) is the position of $\mathcal{B}_j$ in the global cylindrical system. Finally, the scattered potential in the far field is

$$\phi^S = \frac{\pi\mathrm{i}}{kd} \psi_0(z) \sum_{\mu\in\mathcal{M}} \frac{\mathrm{e}^{\mathrm{i}kr\cos(\vartheta-\theta_\mu)}}{\cos\theta_\mu} \sum_{j=1}^{N} \mathrm{e}^{-\mathrm{i}kR_j\cos(\alpha_j-\theta_\mu)} \sum_{n=-\infty}^{\infty} c^j_{0n} \mathrm{e}^{\mathrm{i}n\theta_\mu}. \tag{A 35}$$

Using $\eta_S = \mathrm{i}\omega/g\phi^S(r, \vartheta, 0)$ and comparing the above expression to (2.5), we obtain (4.9), where the expression for the reflected wave amplitudes is obtained by using $\theta^-_\mu = \pi - \theta_\mu$.

https://doi.org/10.1017/jfm.2018.911 Published online by Cambridge University Press

REFERENCES

ABRAMOWITZ, M. & STEGUN, I. A. 1964 *Handbook of Mathematical Functions: with Formulas, Graphs, and Mathematical Tables*. Dover.

ASHCROFT, N. W. & MERMIN, N. D. 1976 *Solid State Physics*. Holt, Rinehart and Winston.

BABARIT, A. 2015 A database of capture width ratio of wave energy converters. *Renew. Energy* **80**, 610–628.

BENNETTS, L. G., PETER, M. A. & CRASTER, R. V. 2018 Graded resonator arrays for spatial frequency separation and amplification of water waves. *J. Fluid Mech.* **854**, R4.

BENNETTS, L. G. & SQUIRE, V. A. 2009 Wave scattering by multiple rows of circular ice floes. *J. Fluid Mech.* **639**, 213–238.

CEBRECOS, A., PICÓ, R., SÁNCHEZ-MORCILLO, V. J., STALIUNAS, K., ROMERO-GARCÍA, V. & GARCIA-RAFFI, L. M. 2014 Enhancement of sound by soft reflections in exponentially chirped crystals. *AIP Adv.* **4** (12), 124402.

CHILD, B. F. M. & VENUGOPAL, V. 2010 Optimal configurations of wave energy device arrays. *Ocean Engng* **37** (16), 1402–1417.

CRASTER, R. V. & GUENNEAU, S. (Eds) 2013 *Acoustic Metamaterials*, vol. 166. Springer.

DREW, B., PLUMMER, A. R. & SAHINKAYA, M. N. 2009 A review of wave energy converter technology. *Proc. Inst. Mech. Engrs* A **223** (8), 887–902.

EVANS, D. V. 1976 A theory for wave-power absorption by oscillating bodies. *J. Fluid Mech.* **77** (01), 1–25.

EVANS, D. V. 1980 Some analytic results for two and three dimensional wave-energy absorbers. In *Power from Sea Waves* (ed. B. M. Count), pp. 213–249. Institute of Mathematics and its Applications, Academic Press.

EVANS, D. V. & PORTER, R. 1997 Near-trapping of waves by circular arrays of vertical cylinders. *Appl. Ocean Res.* **19** (2), 83–99.

EVANS, D. V. & PORTER, R. 1998 Trapped modes embedded in the continuous spectrum. *Q. J. Mech. Appl. Maths* **51** (2), 263–274.

FALNES, J. 1980 Radiation impedance matrix and optimum power absorption for interacting oscillators in surface waves. *Appl. Ocean Res.* **2** (2), 75–80.

FALNES, J. 1984 Wave-power absorption by an array of attenuators oscillating with unconstrained amplitudes. *Appl. Ocean Res.* **6** (1), 16–22.

FALNES, J. & BUDAL, K. 1982 Wave-power absorption by parallel rows of interacting oscillating bodies. *Appl. Ocean Res.* **4** (4), 194–207.

FANO, U. 1941 The theory of anomalous diffraction gratings and of quasi-stationary waves on metallic surfaces (Sommerfeld's waves). *J. Opt. Soc. Am.* **31** (3), 213–222.

GARNAUD, X. & MEI, C. C. 2009 Wave-power extraction by a compact array of buoys. *J. Fluid Mech.* **635**, 389–413.

GARNAUD, X. & MEI, C. C. 2010 Bragg scattering and wave-power extraction by an array of small buoys. *Proc. R. Soc. Lond.* A **466** (2113), 79–106.

GARRETT, C. J. R. 1971 Wave forces on a circular dock. *J. Fluid Mech.* **46** (01), 129–139.

HESSEL, A. & OLINER, A. A. 1965 A new theory of Wood's anomalies on optical gratings. *Appl. Opt.* **4** (10), 1275–1297.

HSU, C. W., ZHEN, B., LEE, J., CHUA, S.-L., JOHNSON, S. G., JOANNOPOULOS, J. D. & SOLJACIC, M. 2013 Observation of trapped light within the radiation continuum. *Nature* **499** (7457), 188–191.

JOANNOPOULOS, J. D., JOHNSON, S. G., WINN, J. N. & MEADE, R. D. 2008 *Photonic Crystals: Molding the Flow of Light*. Princeton University Press.

KAGEMOTO, H. & YUE, D. K. P. 1986 Interactions among multiple three-dimensional bodies in water waves: an exact algebraic method. *J. Fluid Mech.* **166**, 189–209.

LI, Y. & MEI, C. C. 2007*a* Bragg scattering by a line array of small cylinders in a waveguide. Part 1. Linear aspects. *J. Fluid Mech.* **583**, 161–187.

LI, Y. & MEI, C. C. 2007*b* Multiple resonant scattering of water waves by a two-dimensional array of vertical cylinders: linear aspects. *Phys. Rev.* E **76** (1), 016302.

https://doi.org/10.1017/jfm.2018.911 Published online by Cambridge University Press

LINTON, C. M. 1998 The Green's function for the two-dimensional Helmholtz equation in periodic domains. *J. Engng Maths* **33** (4), 377–401.

LINTON, C. M. 2011 Water waves over arrays of horizontal cylinders: band gaps and Bragg resonance. *J. Fluid Mech.* **670**, 504–526.

LINTON, C. M. & MCIVER, P. 2007 Embedded trapped modes in water waves and acoustics. *Wave Motion* **45** (1–2), 16–29.

LINTON, C. M. & THOMPSON, I. 2007 Resonant effects in scattering by periodic arrays. *Wave Motion* **44** (3), 165–175.

MANIAR, H. D. & NEWMAN, J. N. 1997 Wave diffraction by a long array of cylinders. *J. Fluid Mech.* **339**, 309–330.

MARTIN, P. A. 2006 *Multiple Scattering*. Cambridge University Press.

MAYSTRE, D. 2012 Theory of Wood's anomalies. In *Plasmonics* (ed. S. Enoch & N. Bonod), Springer Series in Optical Sciences, vol. 167, pp. 39–83. Springer.

MCIVER, P. 1994 Some hydrodynamic aspects of arrays of wave-energy devices. *Appl. Ocean Res.* **16** (2), 61–69.

MCIVER, P. 2005 Complex resonances in the water-wave problem for a floating structure. *J. Fluid Mech.* **536**, 423–443.

MCIVER, P., LINTON, C. M. & MCIVER, M. 1998 Construction of trapped modes for wave guides and diffraction gratings. *Proc. R. Soc. Lond.* A **454** (1978), 2593–2616.

MCIVER, P. & MCIVER, M. 2007 Motion trapping structures in the three-dimensional water-wave problem. *J. Engng Maths* **58** (1), 67–75.

MEI, C. C., STIASSNIE, M. S. & YUE, D. K. P. 2005 *Theory and Applications of Ocean Surface Waves*. World Scientific.

PETER, M. A. & MEYLAN, M. H. 2009 Water-wave scattering by vast fields of bodies. *SIAM J. Appl. Maths* **70** (5), 1567–1586.

PETER, M. A., MEYLAN, M. H. & LINTON, C. M. 2006 Water-wave scattering by a periodic array of arbitrary bodies. *J. Fluid Mech.* **548**, 237–256.

PORTER, R. & PORTER, D. 2003 Scattered and free waves over periodic beds. *J. Fluid Mech.* **483**, 129–163.

RAYLEIGH, LORD 1907 III. Note on the remarkable case of diffraction spectra described by Prof. Wood. *Lond. Edinb. Dublin Phil. Mag. J. Sci.* **14** (79), 60–65.

SIMON, M. J. 1982 Multiple scattering in arrays of axisymmetric wave-energy devices. Part 1. A matrix method using a plane-wave approximation. *J. Fluid Mech.* **120**, 1–25.

SOMMERFELD, A. 1964 *Partial Differential Equations in Physics*. Academic Press.

SROKOSZ, M. A. 1980 Some relations for bodies in a canal, with an application to wave-power absorption. *J. Fluid Mech.* **99**, 145–162.

STRATIGAKI, V., TROCH, P., STALLARD, T., FOREHAND, D., KOFOED, J., FOLLEY, M., BENOIT, M., BABARIT, A. & KIRKEGAARD, J. 2014 Wave basin experiments with large wave energy converter arrays to study interactions between the converters and effects on other users in the sea and the coastal area. *Energies* **7** (2), 701–734.

TOKIĆ, G. 2016 Optimal configuration of large arrays of floating bodies for ocean wave energy extraction. PhD thesis, Massachusetts Institute of Technology.

TWERSKY, V. 1956 On the scatttering of waves by an infinite grating. *IRE Trans. Antennas Propag.* **4** (3), 330–345.

TWERSKY, V. 1962 On scattering of waves by the infinite grating of circular cylinders. *IRE Trans. Antennas Propag.* **10** (6), 737–765.

WELLER, S. D., STALLARD, T. J. & STANSBY, P. K. 2010 Experimental measurements of irregular wave interaction factors in closely spaced arrays. *IET Renew. Power Gener.* **4** (6), 628–637.

WOOD, R. W. 1902 On a remarkable case of uneven distribution of light in a diffraction grating spectrum. *Phil. Mag.* 6 **4** (21), 396–402.

YEUNG, R. W. 1981 Added mass and damping of a vertical cylinder in finite-depth waters. *Appl. Ocean Res.* **3** (3), 119–133.

https://doi.org/10.1017/jfm.2018.911 Published online by Cambridge University Press